A detailed particle model for polydisperse aggregate particles

Casper S. Lindberg[a,c], Manoel Y. Manuputty[a,c], Edward K. Y. Yapp[b,c], Jethro Akroyd[a,c], Rong Xu[b,c], Markus Kraft[a,b,c,*]

[a]Department of Chemical Engineering and Biotechnology, University of Cambridge, Philippa Fawcett Drive, Cambridge, CB3 0AS, United Kingdom
[b]School of Chemical and Biomedical Engineering, Nanyang Technological University, 62 Nanyang Drive, 6357459, Singapore
[c]Cambridge Centre for Advanced Research and Education in Singapore (CARES), CREATE Tower, 1 Create Way, 138602, Singapore

Abstract

The mathematical description of a new detailed particle model for polydisperse aggregate particles is presented. An aggregate particle is represented as a collection of overlapping spherical primary particles and the model resolves the composition, radius and position coordinates of each individual primary to form a detailed geometrical description of aggregate morphology. Particles transform under inception, coagulation, surface growth, sintering and coalescence processes. The new particle description is used to model the aerosol synthesis of titanium dioxide (TiO_2) aggregates from titanium tetraisopropoxide (TTIP) precursor. TiO_2 particles are formed through collision-limited inception and growth reactions of $Ti(OH)_4$ from the gas-phase, produced from the thermal decomposition of TTIP. Coupling between the particle population balance and detailed gas-phase chemistry is achieved by operator splitting. A numerical study is performed by simulating a simple batch reactor test case to investigate the convergence behaviour of key functionals with respect to the maximum number of computational particles and splitting time step. Finally, a lab-scale hot wall reactor is simulated to demonstrate the advantages of a detailed geometrical description. Simulated particle size distributions were in reasonable agreement with experimental data. Further evaluation of the model and a parametric sensitivity study are recommended.

Keywords: Detailed particle model, Stochastic, Population balance, TTIP,

*Corresponding author
 Email address: mk306@cam.ac.uk (Markus Kraft)

1. Introduction

Population balance models (PBMs) are commonly used to study particulate processes, such as aerosol synthesis. PBMs describe the population dynamics governing the growth of particles and provide a means to investigate the mechanisms controlling the evolution of particle properties. A variety of modelling approaches have been developed in the literature. The particular approach chosen for a modelling study involves two main considerations: the model used to describe the particles and particle processes, and the method employed to solve the population balance equations. The chosen approach should be informed by the nature of the system being modelled and the desired degree of detail. Menz and Kraft [1] emphasise the importance of selecting an appropriate model for the system being simulated, and warn against using an over-simplified model to interpret experimental data. An equally important consideration in selecting a suitable particle model and numerical method is the complexity of the overall system being modelled; for example, spatial inhomogeneity and particle transport. More complex systems typically require the use of computational fluid dynamics and are generally restricted to particle models with fewer internal coordinates due to computational cost.

A range of particle models exist in the literature with varying degrees of detail in the particle description. The simplest, one-dimensional coalescent sphere model [2] describes only the mass, volume or monomer composition of a particle. Two-dimensional models, typically describing a particle by its surface area and volume, can represent a simple aggregate structure and allows sintering to be modelled [3, 4]. Often an assumption of monodisperse primary particles is made to allow primary number and volume to be determined, but bivariate models can also incorporate primary polydispersity [5]. More detailed multivariate models are capable of resolving the mass of individual primary particles, their connectivity [6, 7], and even their detailed internal composition [8]. The most detailed models usually represent an aggregate particle as a union of intersecting spheres [9, 10, 11, 12], providing a full geometrical description of fractal-like particles.

Various methods have been applied to solve the particle population dynamics. These include moment methods [13, 2, 14, 15, 16, 17, 18, 19], sectional methods [20, 21, 3, 22, 23, 24, 5, 25] and stochastic methods [26, 27, 28, 29, 30]. Moment methods are typically fast and easily coupled to gas-phase chemistry and flow dynamics, but do not resolve the particle size distribution (PSD). Sectional methods allow for some resolution of the PSD by dividing

the distribution into a number of sections, but at greater computational expense. Both methods are generally limited to particle models with one or two internal dimensions.

Stochastic methods allow the number of internal dimensions in the particle model to be extended to include a very detailed description of particles. However, these methods can be computationally expensive; and, spatial inhomogeneity and particle transport are not easily incorporated. Thus, detailed population balance models have traditionally been restricted to modelling batch and plug-flow reactors. Although, attempts have been made to apply stochastic methods to systems in which transport effects and spatial inhomogeneity are important. For example, very detailed particle models have been applied to flame simulations using a post-processing methodology. A simple population balance model is first employed in a fully coupled simulation to model the flame profile and capture the coupling of the particle system to the mass and energy balance in the system. The flame data is then post-processed with the detailed particle model. This approach has been used successfully to simulate the internal structure of soot formed in laminar flames [31, 11, 32, 8] and recently extended to stagnation flame synthesised aggregate nanoparticles [33, 34]. Another approach, used to model industrial reactors [35, 36], is to compartmentalise a spatially inhomogeneous system into a network of cells or reactors [37, 38, 39].

Discrete element methods (DEMs) are another useful tool for modelling the evolution of particles with large numbers of interacting primaries. DEMs have been used to perform very detailed studies of particle process dynamics and investigate their effects on the evolution of particle morphology, incorporating a high level of physical detail. Studies have often focussed on understanding the effect of a limited number of processes at one time, such as sintering [12, 40], coagulation [41, 42], and coagulation and surface growth [43, 44]. In addition, DEMs can be combined with stochastic methods to incorporate a specific process description into a detailed population balance model, such as sintering [45].

Population balance models incorporating a detailed particle description provide a powerful tool to investigate the mechanisms that control particle morphology and facilitate the simulation of quantities that are directly comparable to experimental observations. For example, size distributions and mass spectra of particles [46, 8], transmission electron microscopy (TEM) images and optical band gap measurements [32]. Such models also enable the option to include key physical details in the model. For instance, models where the particle growth is a function of the aggregate composition [47, 48], or where sintering and neck growth are resolved for pairs of neighbouring primary particles [49, 50, 6, 51]. Moreover, physical properties are strongly

influenced by particle morphology such as the collision diameter [52], mobility diameter [53, 54], or optical properties [55]; thus, the degree of model detail can a have significant impact on the interpretation of simulation results and comparison with experimental measurements. Models that capture sufficient physical detail also make it possible to further post-process simulation data to study the post-synthesis treatment of particles [56].

In this paper, we develop a new detailed population balance model for polydisperse aggregate particles. The new particle description, or type-space, represents an aggregate particle as a collection of overlapping spheres. This is based on the approach used by Mitchell and Frenklach [9, 10] to model aggregation with surface growth for a single collector particle, and later extended by Morgan et al. [11] to an ensemble of particles. An overlapping spheres model was also employed by Eggersdorfer et al. [12, 40] to simulate multiparticle sintering. We utilise the overlapping spheres approach to model surface growth, sintering, primary particle coalescence and coagulation, incorporating a ballistic cluster-cluster collision model [57] to determine the particle configuration following a coagulation event. The radius, composition and position of each individual primary particle are resolved allowing the morphological evolution of each aggregate to be simulated.

The new model overcomes some of the limitations identified in earlier models [6, 7] while preserving their efficient data structures. These earlier models did not track the coordinates of individual primary particles but rather their connectivity, which required an assumption on the fractal dimension when calculating the radius of gyration and collision diameter, or when simulating a TEM-style image. Furthermore, sintering was resolved by a common surface area for each pair of neighbouring primaries. While this allowed individual necks to sinter at different rates, the model did not account for the effect of sintering on the primary diameter, resolving only a spherical equivalent diameter.

The particle model developed in this work is presented in the context of titanium dioxide (titania, TiO_2) synthesised in flame from titanium tetraisopropoxide (TTIP) precursor – a widely studied system. The underlying type-space and process transformations, however, are general and easily applied to different systems.

Titanium dioxide particles are an important industrial product, manufactured mainly for use in pigments. Aerosol synthesis, typically from titanium tetrachloride ($TiCl_4$) in industry and often from TTIP in lab-scale studies, is a key route for the production of TiO_2 particles. The functionality of the product is strongly influenced by the size, morphology and crystalline phase of the particles. However, despite its commercial importance, a comprehensive understanding of the formation of TiO_2 and the mechanisms that control

the particle properties is still lacking. Thus, the system is of significant interest in detailed modelling studies.

The purpose of this paper is to present the mathematical description of a new particle model; specifically, to give the model equations and describe how the particle geometry is manipulated under individual processes. The algorithms used to effect these changes are also provided. We briefly study the numerical behaviour of the model, investigating the convergence of a number of average properties for a simple batch reactor test case. Finally, we simulate the hot wall reactor experiment of Nakaso et al. [25] to examine some of the features of the model. A more comprehensive evaluation of the model against experimental data and a sensitivity study of the model parameters is proposed for a future work.

2. Detailed chemistry

The chemical model consists of a TTIP decomposition mechanism combined with hydrocarbon combustion chemistry described by the USC-Mech II model [58]. The TTIP decomposition model contains 25 Ti species and 65 reactions, and describes two of the main decomposition pathways identified by Buerger et al. [59]. The decomposition product for both pathways is titanium tetrahydroxide ($Ti(OH)_4$), which is treated as the collision species for the particle inception and growth reactions in the particle model.

3. Particle model

In this section the new detailed particle model is presented. First we describe the particle type-space – the mathematical representation of a particle – followed by the particle processes. Particles evolve through: inception, coagulation, growth, sintering and coalescence. Details on the implementation of the model, including the data structure and algorithms are provided in Appendix A and Appendix B. In this work, the inception and growth processes are assumed to be collision limited reactions consuming $Ti(OH)_4$ from the gas-phase. Relatively simple reactions are chosen to avoid making unnecessary assumptions about the interaction between the gas-phase and particles – an area that is not well understood in the literature. However, the model framework is easy to extend to new inception and growth processes in future studies.

3.1. Type-space

The type-space is the mathematical description of a particle. The detailed particle type-space is illustrated in Fig. 1. An aggregate P_q containing $n_\mathrm{p}(P_q)$
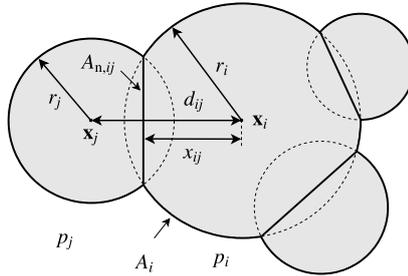
5

Figure 1: An illustration of the detailed particle model type-space. An aggregate particle composed of primary particles (solid lines) modelled as overlapping spheres (indicated by dashed lines).

primary particles, modelled as overlapping spheres [12], is represented by

$$P_q = P_q(p_1, ..., p_{n_{\mathrm{p}}(P_q)}, \mathbf{C}), \tag{1}$$

where a primary particle p_i, with $i \in \{1, ..., n_{\mathrm{p}}(P_q)\}$, is represented by

$$p_i = p_i(\eta_i, r_i, \mathbf{x}_i). \tag{2}$$

η_i is the primary composition and can represent the number of units of TiO_2, as in this work, or could contain a more detailed description of the internal primary structure; for example, the crystal phase composition. r_i is the radius of the primary, and $\mathbf{x}_i$ is the position of the primary centre. It is convenient to express the primary coordinates relative to the centre of mass of the aggregate particle because this simplifies some computations, such as calculating the radius of gyration or performing rotations of the particle during coagulation. For the purpose of calculating the aggregate centre of mass we assume that the primaries are point masses. The degree of overlap between two neighbouring primaries, p_i and p_j, is resolved by their centre to centre separation

$$d_{ij} = |\mathbf{x}_i - \mathbf{x}_j|. \tag{3}$$

The primary particles are stored in a binary tree data structure as in earlier works [6, 7]. The data structure enhances computational performance by allowing very efficient selection of primaries and interrogation of their properties, but does impose some constraints on the primary connectivity within a particle. It would be possible to determine primary connectivity using only the coordinates; however, for the purpose of performing computations the binary tree connectivity is used. A binary tree is ideal for representing branched structures, but closed loops cannot be represented. A closed loop (shown in Fig. 18(b)) is a path that can be taken from a primary that returns to the primary passing through successive neighbours only once.

6

The binary tree is represented in Eq. (1) by the connectivity matrix $\mathbf{C}$. The connectivity matrix is a binary lower triangular matrix of dimension $n_{\mathrm{p}}(P_q) \times n_{\mathrm{p}}(P_q)$ with matrix elements

$$
C_{ij} = \begin{cases} 0, & \text{if } p_i \text{ and } p_j \text{ are not neighbouring;} \\ 1, & \text{if } p_i \text{ and } p_j \text{ are neighbouring.} \end{cases} \tag{4}
$$

The following assumptions are made in the model equations:

1. Neck cross-sections are circular;
2. Neighbours are determined by the binary tree connectivity.

The first assumption implies that the effect of multiple overlaps between primaries (as shown in Fig. A.19) are not considered. This is also a consequence of the second assumption – the binary tree connectivity which does not allow for looped structures. Further detail on the binary tree data structure, connectivity and the assumptions is provided in Appendix A.

Under these assumptions a number of primary particle properties can be derived for the model of overlapping spheres [12]. The volume of a primary p_i is given by the volume of a sphere of radius r_i minus the volume of the caps created by overlaps with its neighbours

$$
\begin{aligned}
v_i &= V_{\mathrm{sph}}(r_i) - \sum_j V_{\mathrm{cap}}(r_i, x_{ij}), \\
&= \frac{4}{3}\pi r_i^3 - \frac{1}{3}\pi \sum_j (2r_i^3 + x_{ij}^3 - 3r_i^2 x_{ij}),
\end{aligned} \tag{5}
$$

where we sum over j neighbours of p_i, and x_{ij} is the distance from the centre of primary p_i to the neck formed with a neighbour p_j

$$
x_{ij} = \frac{d_{ij}^2 - r_j^2 + r_i^2}{2d_{ij}}. \tag{6}
$$

Primary particles are assumed to be composed of units of TiO_2, so $\eta_i = \eta_{TiO_2,i}$, and the volume can also be calculated as

$$
v_i = \frac{\eta_{TiO_2,i} M_{TiO_2}}{\rho_{TiO_2} N_{\mathrm{A}}}, \tag{7}
$$

where M_{TiO_2} is the molar mass of TiO_2, ρ_{TiO_2} is the density of TiO_2 (taken to be that of anatase, $\rho_{TiO_2} = 3.9 \mathrm{~g\,cm}^{-3}$), and N_{A} is the Avogadro constant.

The partial derivatives of v_i give the area of the neck created by the overlap with a neighbour p_j

$$A_{\text{n},ij} = \frac{\partial v_i}{\partial x_{ij}} = \pi(r_i^2 - x_{ij}^2), \qquad (8)$$
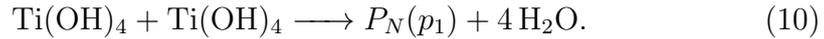
and the free surface area of the primary p_i

$$A_i = \frac{\partial v_i}{\partial r_i} = 4\pi r_i^2 - 2\pi \sum_j (r_i^2 - r_i x_{ij}). \qquad (9)$$

3.2. Particle processes

3.2.1. Inception

Inception is modelled as a bimolecular collision of two Ti(OH)_4 molecules forming a particle consisting of a single spherical primary containing two units of TiO_2:

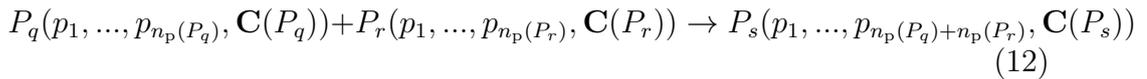$$\text{Ti(OH)}_4 + \text{Ti(OH)}_4 \longrightarrow P_N(p_1) + 4\,\text{H}_2\text{O}. \qquad (10)$$

The rate of inception is calculated using the free molecular kernel:

$$K_{\text{inc}}^{\text{fm}} = \epsilon \sqrt{\frac{\pi k_{\text{B}} T}{m_{\text{Ti(OH)}_4}}} \left(2 d_{\text{Ti(OH)}_4}\right)^2, \qquad (11)$$

where $m_{\text{Ti(OH)}_4}$ and $d_{\text{Ti(OH)}_4}$ are the mass and diameter of a single Ti(OH)_4 molecule respectively. The collision diameter $d_{\text{TiOH}_4} = 0.5128$ nm, is estimated from the geometrical parameters calculated by Buerger et al. [60]. ϵ is the size-dependent collision enhancement factor. Here it is assumed to be size-independent and taken as $\epsilon = 2.2$ as in previous studies on titania [61, 62, 63]. This value is the average size-independent enhancement factor due to van der Waals forces calculated by Harris and Kennedy [64] for spherical soot particles.
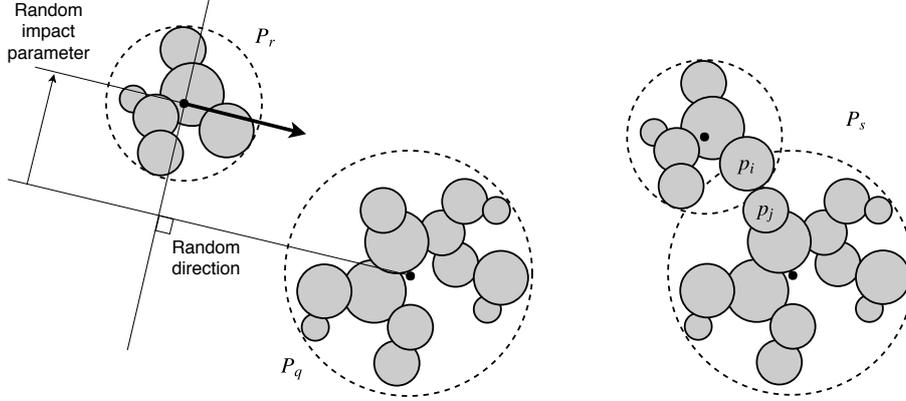
3.2.2. Coagulation

An aggregate is formed when two particles stick together following a collision:

$$P_q(p_1, ..., p_{n_{\text{p}}(P_q)}, \mathbf{C}(P_q)) + P_r(p_1, ..., p_{n_{\text{p}}(P_r)}, \mathbf{C}(P_r)) \rightarrow P_s(p_1, ..., p_{n_{\text{p}}(P_q)+n_{\text{p}}(P_r)}, \mathbf{C}(P_s)) \qquad (12)$$

The rate of coagulation is given by the transition kernel [65]

$$K_{\text{cg}}^{\text{tr}}(P_q, P_r) = \left(\frac{1}{K^{\text{sf}}(P_q, P_r)} + \frac{1}{K^{\text{fm}}(P_q, P_r)}\right)^{-1}, \qquad (13)$$

8

(a) Particles P_r and P_q before collision.

(b) New particle P_s following collision. Point contact between primary p_i from P_r and p_j from P_q.

Figure 2: Ballistic cluster-cluster aggregation with a random impact parameter.

where the slip flow kernel is

$$K^{\text{sf}}(P_q, P_r) = \frac{2k_{\text{B}}T}{3\mu} \left(\frac{1 + 1.257\text{Kn}(P_q)}{d_c(P_q)} + \frac{1 + 1.257\text{Kn}(P_r)}{d_c(P_r)} \right) (d_c(P_q) + d_c(P_r)),$$

(14)

and the free-molecular kernel is

$$K^{\text{fm}}(P_q, P_r) = \epsilon \sqrt{\frac{\pi k_{\text{B}}T}{2} \left(\frac{1}{m(P_q)} + \frac{1}{m(P_r)} \right)} (d_c(P_q) + d_c(P_r))^2.$$

(15)

ϵ is the collision enhancement factor, d_{c} is the particle collision diameter and m is the particle mass. μ is the viscosity of the gas-phase and Kn is the Knudsen number

$$\text{Kn}(P_q) = \frac{2\lambda}{d_c(P_q)},$$

(16)

where λ is the mean free path of the gas. The mean free path and viscosity are approximated as those of air at pressure p and temperature T

$$\lambda = 2.371 \times 10^{-5} \frac{T}{p} \text{ m},$$

(17)

$$\mu = 1.458 \times 10^{-6} \frac{T\sqrt{T}}{T + 110.4} \text{ kg m}^{-1} \text{s}^{-1}.$$

(18)

Once two particles are selected for coagulation based on the rate given by Eq. (13), the orientations and point of contact between the colliding particles are determined by ballistic cluster-cluster aggregation (BCCA) with

9

a random impact parameter [57]. This process is illustrated in Fig. 2. To model a collision three random parameters are generated: the particles are randomly rotated around their centres of mass using the method described by Arvo [66]; a random direction is generated by uniformly picking a point on a sphere centred on one of the particles; and, a random impact parameter is applied by placing the second particle at a random point in the plane perpendicular to the collision direction. The random impact parameter offsets the collision trajectory from the centres of mass. The collision is initialised such that the particle bounding spheres, estimated using the method described by Ritter [67], do not overlap. A detailed algorithm for performing BCCA is given in Appendix B.2.

Following the collision, two primaries p_i and p_j (one from each colliding particle determined by the BCCA algorithm) are assumed to be in point contact and the connectivity is updated as

$$
\mathbf{C}(P_s) = \begin{pmatrix}
 & & & \vdots & & \\
 & \mathbf{C}(P_q) & \cdots & 0 & \cdots \\
 & \vdots & & \vdots & \\
\cdots & C_{ij} & \cdots & \mathbf{C}(P_r) & \\
 & \vdots & & &
\end{pmatrix},
\tag{19}
$$

where $C_{ij} = 1$.

Collision diameter. The diameter of gyration d_g is commonly used as the collision diameter d_c in both the free-molecular and continuum regimes. The diameter of gyration is given by the standard fractal relationship

$$
n_\mathrm{p} = k_\mathrm{f} \left(\frac{d_\mathrm{g}}{d_\mathrm{p,avg}} \right)^{D_\mathrm{f}},
\tag{20}
$$

where $d_\mathrm{p,avg}$ is the average primary diameter, D_f is the fractal dimension and k_f is the fractal pre-factor.

A number of studies [68, 4, 69] employing bivariate models with monodisperse primaries use the fractal relationship to define the collision diameter as

$$
d_\mathrm{c} = d_\mathrm{p} n_\mathrm{p}^{1/D_\mathrm{f}}.
\tag{21}
$$

Kruis et al. [4] note that the characteristics of this collision diameter are:

1. For $n_\mathrm{p} = 1$: the collision diameter is equal to the primary particle diameter.

10

2. For $n_\mathrm{p} \gg 1$: the collision diameter approaches the diameter of gyration of the aggregate.

Lavvas et al. [46] proposed a collision diameter, also based on the fractal relationship, for a multivariate model with polydisperse primaries:

$$d_\mathrm{c} = \left(\frac{6V}{A}\right)\left(\frac{A^3}{36\pi V^2}\right)^{1/D_\mathrm{f}},\tag{22}$$

with

$$A = \frac{A_\mathrm{sph}}{s_\mathrm{avg}(1 - n_\mathrm{p}^{1/3}) + n_\mathrm{p}^{-1/3}},\tag{23}$$

where A_sph is the spherical surface area of the particle and s_avg is the average sintering level of the aggregate.

The drawback of these definitions is that the fractal dimension D_f is a model parameter, typically assumed to be $D_\mathrm{f} \approx 1.8$, and does not evolve as particles grow and sinter. Moreover, the pre-factor is often assumed to be $k_\mathrm{f} \approx 1$ or absorbed into the constant of proportionality between the collision and gyration diameters. In our new model, the ability to track individual primary coordinates permits the diameter of gyration of an individual aggregate to be calculated without assuming a value for k_f and D_f. This can then be used as the collision diameter.

The diameter of gyration is defined [70] as

$$d_\mathrm{g}^2 = \frac{4}{\sum_i m_i}\sum_i m_i(|\mathbf{x}_i|^2 + r_{\mathrm{gp},i}^2),\tag{24}$$

where $r_{\mathrm{gp},i}$ is the radius of gyration of primary p_i and $|\mathbf{x}_i|$ is the distance from the centre of mass of the aggregate to the centre of the primary. For a sphere $r_{\mathrm{gp},i} = \sqrt{5/3}r_i$; however, following Filippov et al. [55] we choose $r_{\mathrm{gp},i} = r_i$, the radius of the primary, so that in the limit of $n_\mathrm{p} = 1$ the collision diameter yields the primary diameter. The collision diameter can then be defined as

$$d_\mathrm{c}^2 = \frac{4}{\sum_i m_i}\sum_i m_i(|\mathbf{x}_i|^2 + r_i^2).\tag{25}$$

In the limit of large n_p this tends to the diameter of gyration. This definition shares the same characteristics of the Eq. (21) as discussed by Kruis et al. [4]. Furthermore, in the case of two primaries of the same size in point contact the collision diameter ($d_\mathrm{c} = 2\sqrt{2}r_\mathrm{p}$) is close to that obtained by Zurita-Gotor and Rosner [52] ($d_\mathrm{c} = 2.892r_\mathrm{p}$).

3.2.3. Growth

Particles can grow by condensation of gas-phase species and surface reactions. In both cases, geometrical adjustments to the particle are performed the same way. In the present application, we consider only a collision limited condensation-like growth process, consuming $Ti(OH)_4$ from the gas-phase and adding TiO_2 to surface of a particle. The rate of collision is based on the free molecular kernel and assumes that the mass and diameter of the condensing species is much smaller than that of the particle

$$K_{cond}^{fm} = \epsilon \sqrt{\frac{\pi k_B T}{2 m_{TiO_2}}} \left(d_c(P_q) \right)^2 . \tag{26}$$

The mass of the condensing species is assumed to be similar to TiO_2.
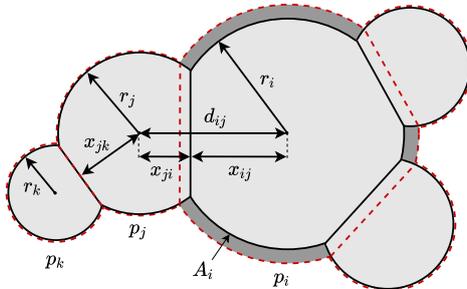

Figure 3: A surface growth event. Mass is added to the free surface of primary p_i (dark shaded region). The new particle geometry is shown by the red dashed line. Immediate neighbours of p_i are labeled p_j, and neighbours of neighbours are labeled p_k.

Fig. 3 shows a particle undergoing a growth event. A primary, p_i, is selected with probability proportional to its relative free surface area, $A_i/A(P_q)$. The condensing mass is added to the free surface of p_i (shaded region in Fig. 3) increasing the primary radius r_i. We assume that the primary positions $\mathbf{x}_i$, and all other primary radii r_j remain unchanged during the event. The change in radius given a change in the aggregate particle volume $V(P_q)$ is

$$\frac{dr_i}{dt} = \frac{1}{A_i} \frac{dV(P_q)}{dt}. \tag{27}$$

Following a growth event, the positions of the necks between p_i and its neighbours p_j will have changed as illustrated by the red dashed lines in Fig. 3. This amounts to a redistribution of mass between primaries and requires an adjustment to the compositions of p_i and its neighbours p_j. The adjustment is performed in discrete units of TiO_2, with unit volume

$$v_{TiO_2} = \frac{M_{TiO_2}}{\rho_{TiO_2} N_A}. \tag{28}$$

The change in volume of a neighbour p_j is

$$\frac{\mathrm{d}v_j}{\mathrm{d}t} = \frac{\partial v_j}{\partial r_j}\frac{\mathrm{d}r_j}{\mathrm{d}t} + \sum_k \frac{\partial v_k}{\partial x_{jk}}\frac{\mathrm{d}x_{jk}}{\mathrm{d}t}, \tag{29}$$

where we sum over the neighbours p_k of primary p_j. Under the assumption that the radius of p_j remains constant and noting that the position of the neck between p_j and some other neighbour p_k ($k \neq i$) does not change, this is reduced to

$$\frac{\mathrm{d}v_j}{\mathrm{d}t} = A_{\mathrm{n},ji}\frac{\mathrm{d}x_{ji}}{\mathrm{d}t}, \tag{30}$$

where we have used Eq. (8). Under the same assumptions, differentiating Eq. (6), allows the change in volume of p_j to be expressed in terms of the change in the radius of p_i:

$$\frac{\mathrm{d}v_j}{\mathrm{d}t} = -A_{\mathrm{n},ij}\frac{r_i}{d_{ij}}\frac{\mathrm{d}r_i}{\mathrm{d}t}. \tag{31}$$

from which the integer change in composition of p_j can be determined:

$$\Delta\eta_{\mathrm{TiO_2},j} = \frac{\Delta v_j}{v_{\mathrm{TiO_2}}}. \tag{32}$$

The surface adjustment algorithm and a discussion of the consequence of limiting the mass redistribution to discrete unit changes can be found in Appendix B.3.
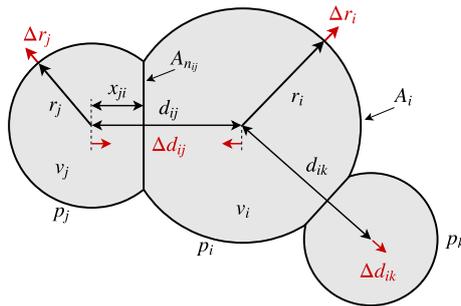
3.2.4. Sintering

Figure 4: Sintering of a single neck between primaries p_i and p_j. Neighbours not sintering are labelled p_k. The centre to centre separation decreases by Δd_{ij}. To conserve mass, the radii of the sintering primaries increase by Δr_i and Δr_j respectively and the separation with neighbouring primary p_k increases by Δd_{ik}.

Sintering is performed on each neck individually. A single sintering event on primaries p_i and p_j is shown in Fig. 4. The centres of primaries p_i and p_j approach each other, increasing their overlap and neck radius. For titania particles the sintering rate is evaluated using a grain boundary diffusion model [40]. Mass conservation requires that the primary radii r_i and r_j increase. It is assumed that all other neighbours p_k and their respective necks remain unchanged during the event. This requires that the separation d_{ik} increases in response to the change in r_i.

Grain Boundary Diffusion.. Following Eggersdorfer et al. [40], the change in distance from the centre of p_i to the neck formed with p_j is

$$\frac{\mathrm{d}x_{ij}}{\mathrm{d}t} = -\frac{2\pi D_\mathrm{v} C_\mathrm{v0} \delta_\mathrm{gb} \gamma \Omega}{k_\mathrm{B} T A_{\mathrm{n},ij}} \left(\frac{1}{r_i - x_{ij}} - \frac{1}{R_{ij}} \right), \tag{33}$$

where R_{ij} is the neck radius, $A_{\mathrm{n},ij}$ is the neck area, and r_i is the primary radius. The product of the vacancy diffusion coefficient, D_v, the equilibrium vacancy concentration, C_v0, and grain boundary thickness, δ_gb, is taken from Astier and Vergnon [71],

$$D_\mathrm{v} C_\mathrm{v0} \delta_\mathrm{gb} = 1.6 \times 10^{-14} \exp\left(\frac{-258 \text{ kJ mol}^{-1}}{RT} \right) \text{ m}^3 \text{ s}^{-1}. \tag{34}$$

The surface free energy, $\gamma = 0.6$ J m^{-2}, and vacancy volume, $\Omega = 1.57 \times 10^{-29}$ m^3, are from Anderson [72].

The rate of change in centre to centre separation is

$$\begin{aligned}
\frac{\mathrm{d}d_{ij}}{\mathrm{d}t} &= \frac{\mathrm{d}x_{ij}}{\mathrm{d}t} + \frac{\mathrm{d}x_{ji}}{\mathrm{d}t}, \\
&= \frac{-6.859 \times 10^{-20}}{T A_{\mathrm{n},ij}} \left(\frac{1}{r_i - x_{ij}} + \frac{1}{r_j - x_{ji}} - \frac{2}{R_{ij}} \right) \\
&\quad \cdot \exp\left(\frac{-258 \text{ kJ mol}^{-1}}{RT} \left(1 - \frac{d_{\mathrm{p,crit}}}{\min(d_{\mathrm{p},i}, d_{\mathrm{p},j})} \right) \right).
\end{aligned} \tag{35}$$

Here we have introduced a critical sintering diameter $d_{\mathrm{p,crit}}$ into the exponential term, of a form similar to that first introduced by Tsantilis et al. [73] for silica, to allow effectively instantaneous coalescence of primaries with $d_\mathrm{p} < d_{\mathrm{p,crit}}$. Rapid coalescence of very small particles is consistent with findings from molecular dynamics studies [74], and has also been suggested in other works [75]. Buesser et al. [74] found that primaries with $d_\mathrm{p} < 4$ nm sinter significantly faster than what would be predicted by the models of Kobata et al. [76] and Seto et al. [75]. In this work we use $d_{\mathrm{p,crit}} = 4$ nm.

Conservation of mass. Assuming that the density does not change, mass conservation implies that primary particle volume is conserved. The volume conservation of primary p_i is [12]

$$\frac{\mathrm{d}v_i}{\mathrm{d}t} = \frac{\partial v_i}{\partial r_i}\frac{\mathrm{d}r_i}{\mathrm{d}t} + \sum_k \frac{\partial v_i}{\partial x_{ik}}\frac{\mathrm{d}x_{ik}}{\mathrm{d}t} = 0, \tag{36}$$

where p_k is some neighbour of p_i. Rearranging and substituting Eqs (8) and (9):

$$\frac{\mathrm{d}r_i}{\mathrm{d}t} = \frac{-\sum_k A_{\mathrm{n},ik}\frac{\mathrm{d}x_{ik}}{\mathrm{d}t}}{A_i}. \tag{37}$$

The time derivative of x_{ik}, the distance from the centre of p_i to the neck with a neighbour p_k, is

$$\frac{\mathrm{d}x_{ik}}{\mathrm{d}t} = \frac{r_i}{d_{ik}}\frac{\mathrm{d}r_i}{\mathrm{d}t} - \frac{r_k}{d_{ik}}\frac{\mathrm{d}r_k}{\mathrm{d}t} + \left(1 - \frac{x_{ik}}{d_{ik}}\right)\frac{\mathrm{d}d_{ik}}{\mathrm{d}t}. \tag{38}$$

For $k \neq j$ (i.e. a neighbour not sintering)

$$\frac{\mathrm{d}r_k}{\mathrm{d}t} = 0 \quad \text{and} \quad \frac{\mathrm{d}x_{ki}}{\mathrm{d}t} = 0. \tag{39}$$

Eq. (38) can then be reduced to

$$\begin{aligned}
\frac{\mathrm{d}x_{ik}}{\mathrm{d}t} &= \frac{r_i}{d_{ik}}\frac{\mathrm{d}r_i}{\mathrm{d}t} + \left(1 - \frac{x_{ik}}{d_{ik}}\right)\frac{\mathrm{d}x_{ik}}{\mathrm{d}t}, \\
&= \frac{r_i}{x_{ik}}\frac{\mathrm{d}r_i}{\mathrm{d}t} \quad \text{for } k \neq j,
\end{aligned} \tag{40}$$

and Eq. (37) becomes

$$\begin{aligned}
\frac{\mathrm{d}r_i}{\mathrm{d}t} &= \frac{-A_{\mathrm{n},ij}\frac{\mathrm{d}x_{ij}}{\mathrm{d}t} - \sum_{k \neq j} A_{\mathrm{n},ik}\frac{r_i}{x_{ik}}\frac{\mathrm{d}r_i}{\mathrm{d}t}}{A_i}, \\
&= \frac{-A_{\mathrm{n},ij}}{B_{ij}}\frac{\mathrm{d}x_{ij}}{\mathrm{d}t}, \\
&= \frac{-A_{\mathrm{n},ij}}{d_{ij}B_{ij} + r_i A_{\mathrm{n},ij}}\left(-r_j\frac{\mathrm{d}r_j}{\mathrm{d}t} + x_{ji}\frac{\mathrm{d}d_{ij}}{\mathrm{d}t}\right),
\end{aligned} \tag{41}$$

where

$$B_{ij} = A_i + \sum_{k \neq j} A_{\mathrm{n},ik}\frac{r_i}{x_{ik}}, \tag{42}$$

$$\tag{43}$$

15

A similar expression can be derived for r_j

$$\frac{\mathrm{d}r_j}{\mathrm{d}t} = \frac{-A_{\mathrm{n},ij}}{d_{ij}B_{ji} + r_j A_{\mathrm{n},ij}} \left(-r_i \frac{\mathrm{d}r_i}{\mathrm{d}t} + x_{ij} \frac{\mathrm{d}d_{ij}}{\mathrm{d}t} \right). \tag{44}$$

Combining Eqs (41) and (44) gives the change in radius as a function of the change in centre to centre separation:

$$\frac{\mathrm{d}r_i}{\mathrm{d}t} = \frac{-r_j A_{\mathrm{n},ij}^2 - x_{ji}B_{ji}A_{\mathrm{n},ij}}{d_{ij}B_{ij}B_{ji} + r_j A_{\mathrm{n},ij}B_{ij} + r_i A_{\mathrm{n},ij}B_{ji}} \frac{\mathrm{d}d_{ij}}{\mathrm{d}t}. \tag{45}$$

The centre to centre separations of neighbours not sintering are adjusted according to Eq. (40). The sintering algorithm is presented in Appendix B.4.

3.2.5. Coalescence

(a) Before merger. (b) After merger.
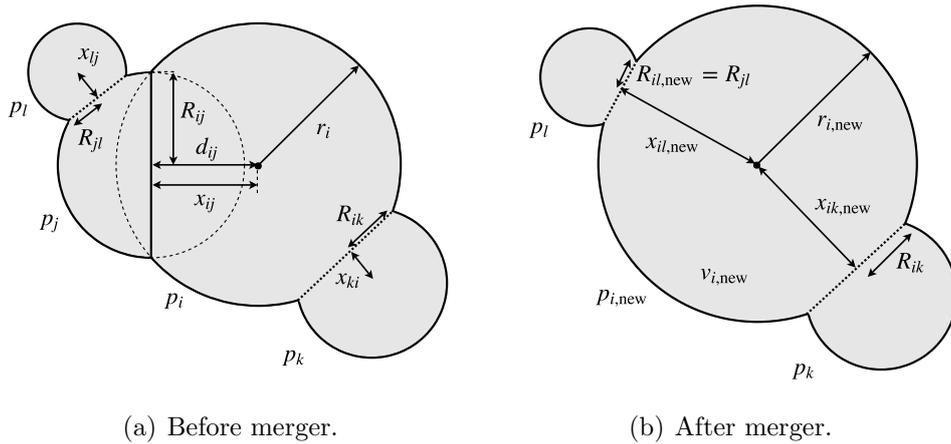
Figure 5: Primary particle coalescence. Primary p_j is merged into p_i. Neighbours of p_j are added to p_i preserving the neck radius.

The sintering level for a neck is defined as the ratio of the neck radius to the radius of the smaller primary

$$s_{ij} = \frac{R_{ij}}{r_j} \qquad \text{where} \quad r_j \leq r_i. \tag{46}$$

Note that $0 \leq s_{ij} \leq 1$. Both sintering and growth increase the sintering level. Once the sintering level exceeds 0.95, the two primaries are assumed to have coalesced into a single primary. Two primaries, p_i and p_j, are shown coalescing in Fig. 5. During a coalescence event the smaller primary, in this case p_j, is merged into the larger primary p_i. The other neighbour of p_j,

labelled p_l, is added to the new merged primary preserving the neck radius such that $R_{ik,\text{new}} = R_{jl}$. The primary is translated along vector $\mathbf{x}_l - \mathbf{x}_i$ to its new position. The other neighbour of p_i, labelled p_k, also preserves its neck radius.

Following the merger, the radius of p_i has changed to $r_{i,\text{new}}$, which requires the neighbour separations to be recalculated since we assume the neighbours are unchanged by the merger. The volume of the new merged primary is

$$v_{i,\text{new}} = v_i + v_j, \tag{47}$$

and expressed in terms of the new radius, the volume (Eq. (5)) is

$$v_{i,new} = \frac{4}{3}\pi r_{i,\text{new}}^3 + \frac{\pi}{3} \sum_{m \in \{k,l\}} \left(2r_{i,\text{new}}^3 + \left(r_{i,\text{new}}^2 - \frac{A_{n,im}}{\pi} \right)^{3/2} - 3r_{i,\text{new}}^2 \left(r_{i,\text{new}}^2 - \frac{A_{n,im}}{\pi} \right) \right), \tag{48}$$

where we sum over all the neighbours, p_k and p_l, of new merged primary $p_{i,\text{new}}$. Equation (48) is solved for $r_{i,\text{new}}$ using the Newton-Raphson method and the new primary separation can be determined using Eq. (6). For more detail on the merger algorithm refer to Appendix B.5

4. Numerical method

The detailed population balance equations are solved using a stochastic numerical method: a direct simulation algorithm with various enhancements to improve efficiency. The method uses a majorant kernel and fictitious jumps [26, 27, 65] to improve the computational speed of calculating the coagulation rate. A linear process deferment algorithm (LPDA) [29] is used to provide an efficient treatment of the sintering and growth processes. The direct simulation Monte-Carlo algorithm (DSA) is presented in Appendix B.

Coupling of the particle population balance to the gas-phase chemistry, solved using an ODE solver, is achieved by the operator splitting technique described by Celnik et al. [77]. The technique employs a refinement introduced by Strang [78], which staggers the two operators by half a splitting time step, $\Delta t_{\text{s}}/2$.

The population balance solver uses a variable size particle ensemble with a predefined maximum number of computational particles N_{max}. The particle ensemble represents a real population of particles contained in a sample volume

$$V_{\text{smpl}} = \frac{N}{M_0}. \tag{49}$$

The sample volume is adjusted due to gas-phase expansion and contraction, and ensemble contraction and doubling. Ensemble contractions occur when a

new particle is incepted into an already saturated ensemble. Since the maximum ensemble size $N_{\max}$ cannot be adjusted during simulation a random particle is discarded instead and the sample volume is contracted proportionately to represent a smaller volume in the real system. Contractions, however, results in a loss of information and can significantly alter the particle size distribution. Therefore, it is important to select an appropriate initial sample volume size to minimise the number of contractions. This is done by estimating the maximum value of the particle number density over the course of the simulation, $M_{0,\max}$, such that initially

$$V_{\mathrm{smpl}} = \frac{N_{\max}}{M_{0,\max}}. \tag{50}$$

To maintain a statistically significant number of computational particles, the ensemble is doubled if $N(t) < N_{\max}/2$. In this case, each computational particle is duplicated and the sample volume is doubled. Therefore, during the simulation (except at early times) the actual number of computational particles lies approximately in the range $[N_{\max}/2, N_{\max}]$.

5. Numerical studies

The numerical behaviour of the model is investigated using a simple test case. A zero-dimensional batch reactor was simulated with 500 ppm of titanium tetraisopropoxide (TTIP) precursor in nitrogen gas. The temperature was kept constant at 1200 K and the pressure at 1 atm. The reactor residence time was 0.5 s. These conditions were chosen to yield a reasonable degree of aggregation and sintering to fully demonstrate the model. Simulations were performed on 2.80 GHz Intel® Xeon® CPUs.

The numerical parameters that affect the numerical error are:

- Maximum number of computational particles ($N_{\max}$);

- Number of runs (L);

- Splitting time step (Δt_{s}).

First, we look at the convergence behaviour with respect to the splitting time step in order to select an appropriate splitting time for the rest of the study. Then we investigate the convergence of six macroscopic properties with respect to to the maximum number of computational particles $N_{\max}$, while keeping $N_{\max} \times L$ constant. The functionals studied are given in Table 1.

Table 1: Functionals studied

Functional	Formula
Zeroth moment	$M_0(t) = \dfrac{N(t)}{V_{\text{smpl}}(t)}$
Volume fraction	$F_v(t) = \dfrac{1}{V_{\text{smpl}}(t)} \displaystyle\sum_{q=1}^{N(t)} V(P_q(t))$ V: aggregate volume
Average collision diameter	$\bar{d}_c(t) = \dfrac{1}{N(t)} \displaystyle\sum_{q=1}^{N(t)} d_c(P_q(t))$ d_c defined in Eq. (25).
Average number of primaries per particle	$\bar{n}_p(t) = \dfrac{1}{N(t)} \displaystyle\sum_{q=1}^{N(t)} n_p(P_q(t))$ $n_p(P_q)$: number of primaries in P_q
Average primary diameter	$\bar{d}_p(t) = \dfrac{1}{N(t)} \displaystyle\sum_{q=1}^{N(t)} d_{p,\text{avg}}(P_q(t))$ $d_{p,\text{avg}}(P_q)$: average primary diameter of P_q
Average sintering level	$\bar{s}(t) = \dfrac{1}{N(t)} \displaystyle\sum_{q=1}^{N(t)} s_{\text{avg}}(P_q(t))$ $s_{\text{avg}}(P_q)$: mean sintering level of P_q

5.1. Error calculations

The systematic and statistical errors can be assessed by generating L independent estimates of the particle system and comparing the macroscopic quantities of the system $\xi_l(t)$ for a given set of parameters. The empirical mean at time t is

$$\mu_1(t) = \frac{1}{L} \sum_{l=1}^{L} \xi_l(t), \qquad (51)$$

and the variance is

$$\mu_2(t) = \frac{1}{L} \sum_{l=1}^{L} [\xi_l(t)]^2 - [\mu_1(t)]^2 . \qquad (52)$$

The half-width of the confidence interval for $\mu_1(t)$ is calculated using the central limit theorem:

$$c_P(t) = a_P \sqrt{\frac{\mu_2(t)}{L}}. \tag{53}$$

For a confidence level of $P = 0.999$, a critical value of $a_P = 3.29$ is obtained from the standard normal distribution. The confidence interval I_P within which there is a probability P of finding the solution is then given by

$$I_P(t) = [\mu_1(t) - c_P(t), \mu_1(t) + c_P(t)]. \tag{54}$$

The relative error at time t is

$$e_{\mathrm{r}}(t) = \frac{|\mu_1(t) - \zeta(t)|}{\zeta(t)} \tag{55}$$

where $\zeta(t)$ is an approximation for the true solution which is obtained from a high-precision calculation with a very large number of particles. In this case, $N_{\mathrm{max}} = 2^{17}$ and $L = 10$ is used. The total relative error, averaged over M time steps is

$$e_{\mathrm{tot}} = \frac{1}{t_{\mathrm{res}}} \sum_{j=1}^{M} e_{\mathrm{r}}(t_j) \Delta t_j, \tag{56}$$

where

$$t_{\mathrm{res}} = \sum_{j=1}^{M} \Delta t_j. \tag{57}$$

5.2. Numerical results

5.2.1. Convergence with respect to splitting time step

The length of the operator splitting time step size Δt_{s} affects the accurancy and stability of the coupling between the gas-phase and particle population balance. If the time step is too long, the operator splitting can cause unphysical oscillations to arise in the concentrations of species that have source terms in the gas-phase and sink terms in the particle-phase (or vice versa). For example, $\mathrm{Ti(OH)_4}$ is first formed in the gas-phase as a product of the decomposition of TTIP and then consumed by the particle phase as the inception and growth species. On the other hand, taking unnecessarily small time steps when species concentrations are varying slowly increases the computational time due to the cost of initialising the ODE solver. Thus, an appropriate time step needs to be chosen to maintain adequate coupling while keeping computational cost at a minimum.

The convergence behaviour with respect to the splitting time step of three key particle ensemble properties (M_0, F_v and $\bar{d}_{\mathrm{c}}$) and the concentration of

$Ti(OH)_4$, the collision species, is investigated. Simulations were performed with a sufficiently large number of particles and number of runs for convergence: $N_{max} = 8192$ and $L = 4$. The relative error is measured against a high precision solution: $N_{max} = 131072$, $L = 10$ and Δt_s given by the variable splitting time scheme discussed below.
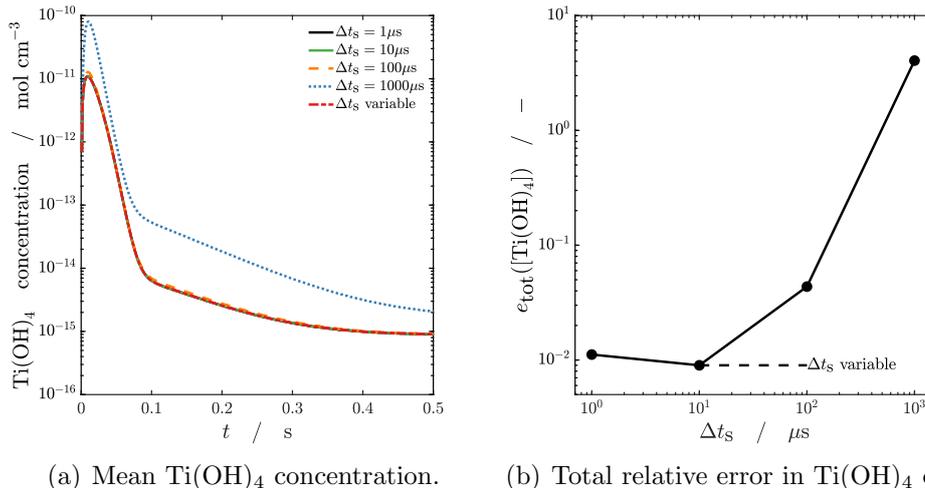

(a) Mean $Ti(OH)_4$ concentration.   (b) Total relative error in $Ti(OH)_4$ conc.

Figure 6: Mean $Ti(OH)_4$ concentration as a function of time and the total relative error for different splitting step sizes. The horizontal dashed line indicates the value for the variable splitting scheme (Eq. (58)).

Figure 6 shows the time evolution and the total relative error of the concentration of $Ti(OH)_4$ for different splitting time step sizes. The solution converges rapidly with decreasing step size and appears converged with $\Delta t_s = 10$ μs. Figure 6(a) shows that the collision species is consumed rapidly and its concentration becomes negligible by $t = 0.1$ s. This suggests that a small splitting time step is only necessary during this initial phase of the simulation where there is a strong coupling between the gas-phase and particle-phase. Once the precursor and collision species have been consumed a longer time step can be taken. The dashed horizontal line in Fig. 6(b) shows the total relative error for a variable splitting time scheme in which the step size is increased after $t = 0.1$ s:

$$\Delta t_s = \begin{cases} 10 \ \mu s, & t \leq 0.1 \text{ s}; \\ 100 \ \mu s, & t > 0.1 \text{ s}. \end{cases} \tag{58}$$

The variable splitting scheme achieves the same total relative error as $\Delta t_s = 10$ μs.
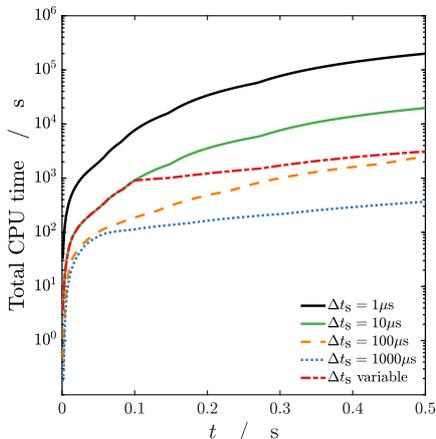
Figure 7: Computational time as a function of simulation time for different splitting time steps. Variable refers to the splitting scheme given in Eq. (58).

The computational time for one run using each of the different step sizes is shown in Fig. 7. There is a clear increase in computational cost with decreasing step size: almost an order of magnitude increase in CPU time with an order magnitude decrease in step size. The CPU time for the variable step size (Eq. (58)) is also shown, and demonstrates a significant reduction in computational cost compared to the $\Delta t_{\rm s} = 10$ μs case for approximately the same total error.

Figure 8 shows the convergence behaviour of M_0, F_v and $\bar{d}_{\rm c}$ with respect to splitting step size. Similar convergence behaviour is observed for these functionals as for the concentration of Ti(OH)$_4$, with all converging by $\Delta t_{\rm s} = 10$ μs. The variable splitting scheme (Eq. (58)) shows similar convergence properties to $\Delta t_{\rm s} = 10$ μs. Due to the computational time advantage, this splitting scheme was selected for the remaining numerical studies.

5.2.2. Convergence with respect to number of particles

The maximum number of computational particles should be chosen such that systematic error is sufficiently small. In practice this means choosing the maxmimum number of computational particles so that increasing $N_{\rm max}$ is not statistically significant. The number of runs is selected such that the statistical error is acceptable. The convergence behaviour of the functionals given in Table 1 was investigated with respect to the maximum number of computational particles $N_{\rm max}$, while keeping the product of the number of computational particles and number of runs constant: $N_{\rm max} \times L = 2^{17}$.
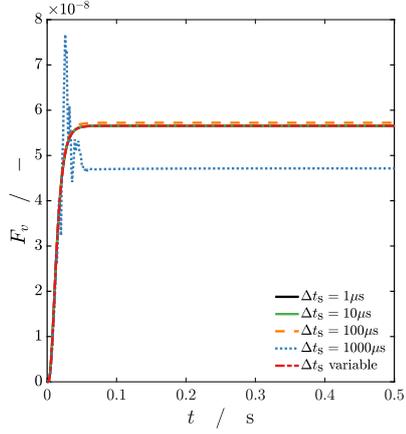
The time evolution of each of the functionals within their confidence intervals $I_{\rm P}(t)$ is shown in Fig. 9 for three different values of $N_{\rm max}$ and the high
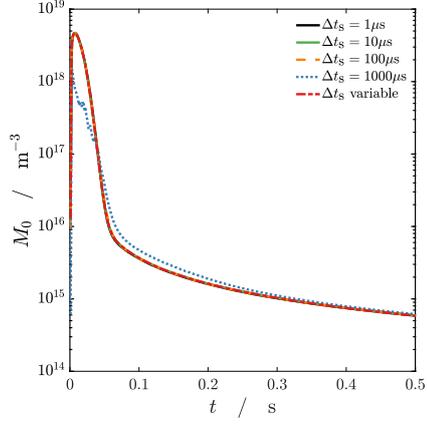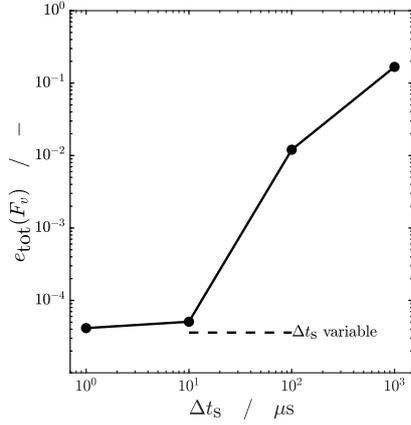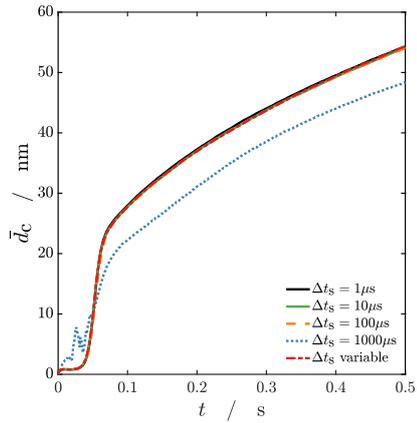
(a) Mean number density, M_0.
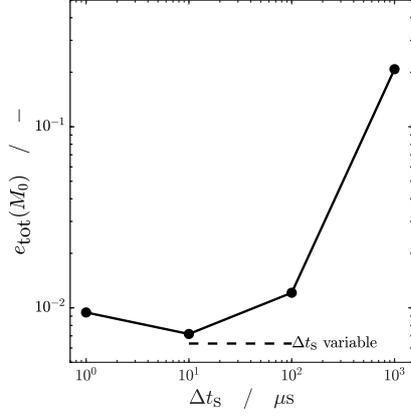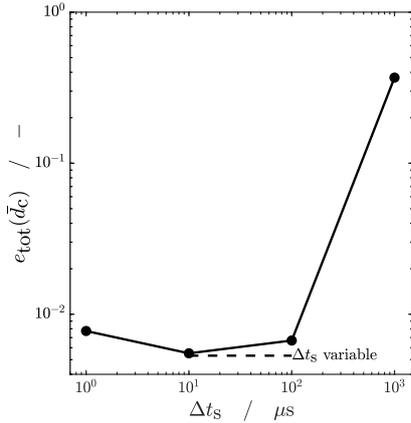
(b) Total relative error in M_0.

(c) Mean volume fraction, F_v.

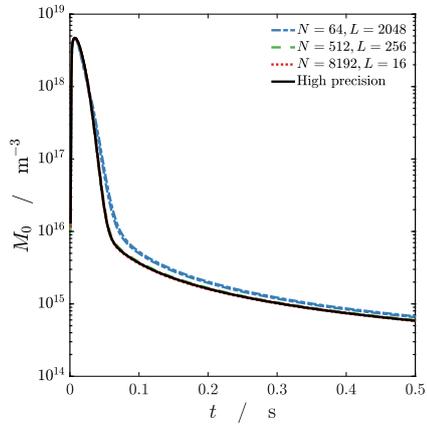(d) Total relative error in F_v.

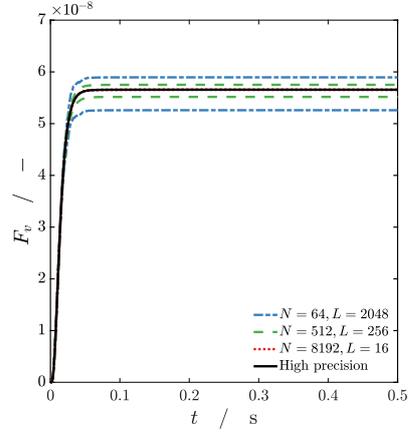(e) Mean collision diameter, $\bar{d}_c$.
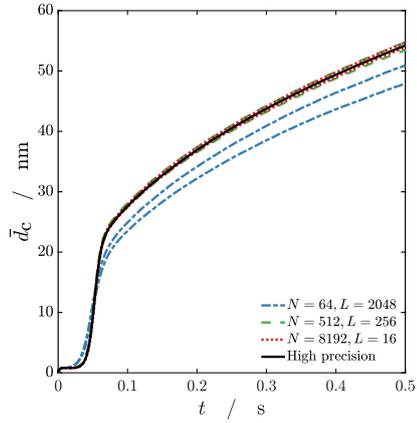
(f) Total relative error in $\bar{d}_c$.

Figure 8: Mean functional value as a function of time and the total relative error for different splitting step sizes. The horizontal dashed line is the variable splitting scheme (Eq. (58)).

23

(a) Number density, M_0.

(b) Volume fraction, F_v.

(c) Average collision diameter, $\bar{d}_{\mathrm{c}}$.
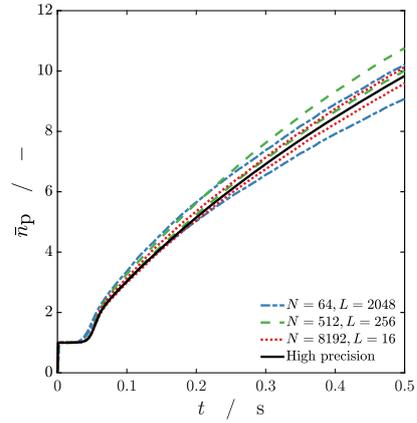
(d) Average number of primaries, $\bar{n}_{\mathrm{p}}$.
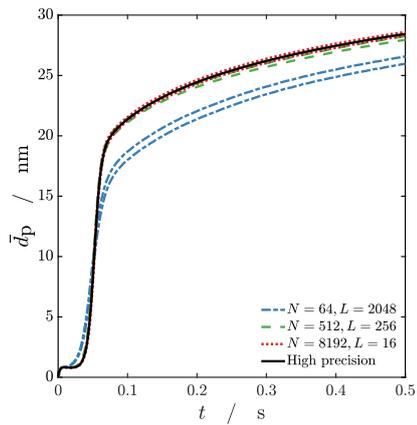
(e) Average primary diameter, $\bar{d}_{\mathrm{p}}$.
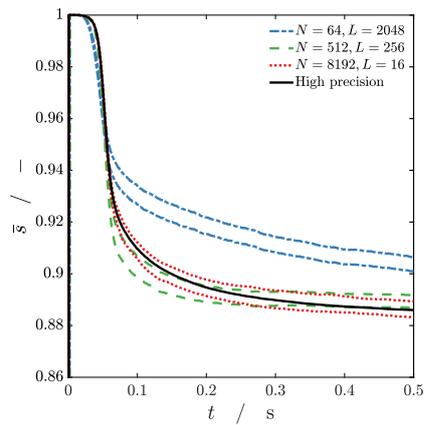
(f) Average sinteirng level, $\bar{s}$.

Figure 9: Time evolution of functionals given in Table 1 within their confidence intervals $I_{\mathrm{P}}(t)$ for different values of $N_{\max}$, and the high precision solution.

precision solution. The evolution of M_0 and F_v indicate the rapid conversion of gas-phase precursor to TiO_2 in the particle phase. There is an initial spike in M_0 as many small single primary particles are incepted, followed by a rapid decrease in M_0 and corresponding increase in $\bar{d}_p$ and $\bar{d}_c$ as particles grow via condensation and coalescence. Aggregate formation, shown by the increase in $\bar{n}_p$, begins after F_v has plateaued i.e. the gas-phase precursor has been consumed, and once the primary size exceeds the critical sintering diameter. At this point primary diameter growth slows and further growth is due to sintering. The initial sintering level is $\bar{s} = 1$: the value assigned to single primaries. Once aggregates begin to form the average sintering level falls rapidly before plateauing at around $\bar{s} = 0.886$.

The functionals plotted in Fig. 9 display different rates of convergence with respect to the maximum number of computational particles and different statistical errors as evidenced by the width of the confidence intervals. For example, M_0 shows very rapid convergence to the high precision solution and small statistical error, while F_v also displays rapid convergence but larger statistical error. On the other hand, the average sintering level $\bar{s}$ and average number of primaries $\bar{n}_p$ both demonstrate a slower rate of convergence and larger statistical error.

The rates of convergence with respect to the maximum number of computational particles of the functionals are investigated further in Fig. 10: a plot of the total relative error e_{tot} as a function of N_{max}. A first order slope is also plotted as a guide. All the functionals are observed to converge as N_{max} is increased. The volume fraction displays the smallest total error, likely due to the fact that the gas-phase precursor is consumed rapidly and F_v reaches a steady value within the first 0.1 s as seen in Fig. 9(b). The ensemble properties M_0 and F_v, and average collision diameter $\bar{d}_c$ are the fastest to converge at $N_{max} = 2048$. The average number of primaries $\bar{n}_p$ shows the slowest convergence at $N_{max} = 8192$.

The computational times for a single run with different values of N_{max} are plotted in Fig. 11 together with the total relative error for M_0, $\bar{n}_p$ and $\bar{s}$. The total computational time and computational time of the Monte-Carlo algorithm are shown. The CPU time of the Monte-Carlo algorithm increases steadily as a function N_{max}. The total CPU time, however, is constant for small N_{max}. At low N_{max}, changing the number of particles does not affect the total computational time very much because most of the CPU time is spent on the ODE solver, which is independent of the number of computational particles. For large N_{max} the majority of the computational time is spent on the Monte-Carlo algorithm. M_0 converges the fastest with $N_{max} = 2048$ in approximately 9 min, while $\bar{n}_p$ is the slowest, converging with approximately $N_{max} = 8192$ in 27 min.
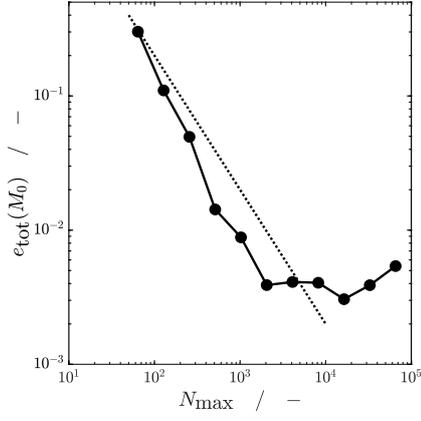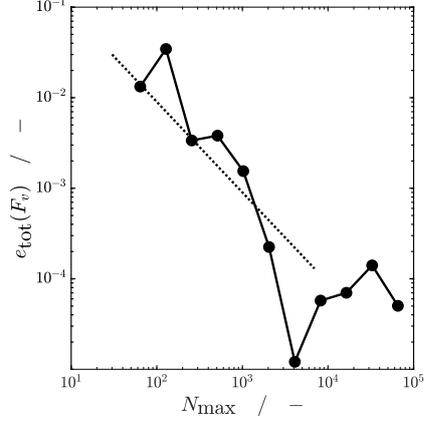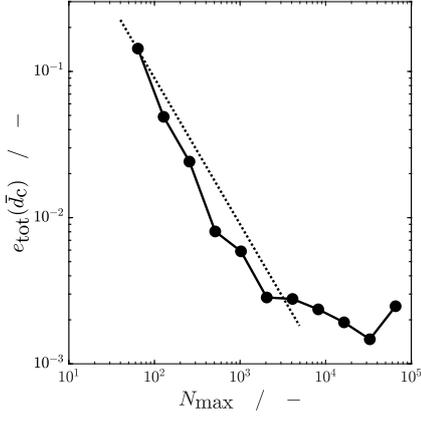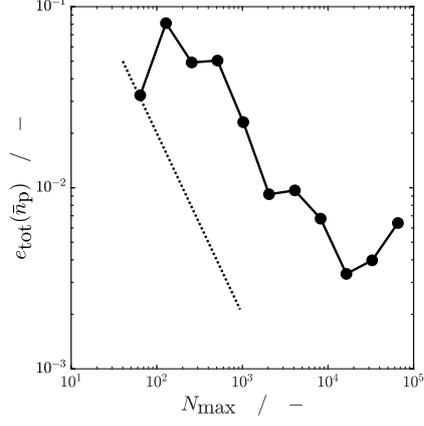
25

(a) Number density, M_0.

(b) Volume fraction, F_v.

(c) Average collision diameter, $\bar{d}_{\mathrm{c}}$.

(d) Average number of primaries, $\bar{n}_{\mathrm{p}}$.
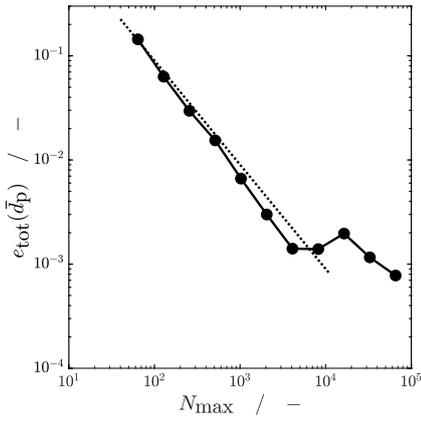
(e) Average primary diameter, $\bar{d}_{\mathrm{p}}$.
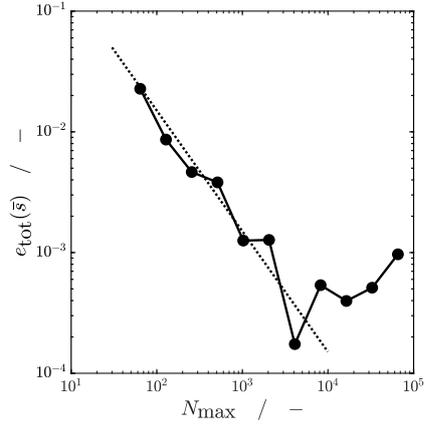
(f) Average sinteirng level, $\bar{s}$.

Figure 10: Total relative error as a function of $N_{\max}$ for the functionals given in Table 1. $N_{\max} \times L = 2^{17}$ is kept constant. A first order slope (dotted line) is plotted as a guide.
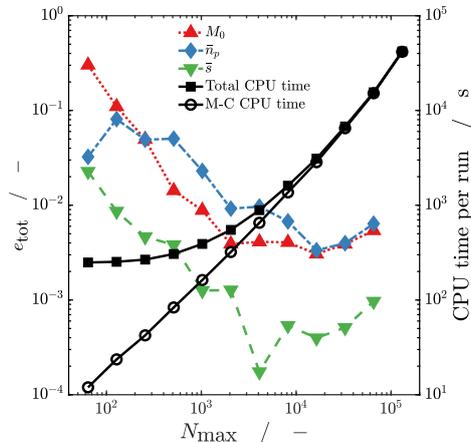
Figure 11: Total and Monte-Carlo algorithm CPU time per run (RHS), and total relative error for number density M_0, average number of primaries $\bar{n}_\mathrm{p}$ and average sintering level $\bar{s}$ (LHS) for different values of N_max.

6. Hot wall reactor simulations

In this section we simulate the hot wall reactor experiment of Nakaso et al. [25]. The original investigation produced TiO_2 particles from TTIP precursor evaporated into nitrogen carrier gas in a tubular hot wall flow reactor. In our simulation we impose the temperature profile modelled by Nakaso et al. [25, Fig. 4] for maximum furnace temperature $T_\mathrm{max} = 1200°C$. The temperature profile is expressed in terms of reactor residence time by assuming constant mass flow and accounting for the thermal expansion of the gas-phase. The initial TTIP mole fraction was calculated as 18.7 ppm for an initial concentration of 7.679×10^{-7} mol/l in nitrogen gas at 24°C and 1 atm. The total reactor residence time was calculated to be $t_\mathrm{res} = 3.60$ s.

6.1. Time evolution

Figure 12 shows the simulated time evolution of key gas-phase species, the imposed temperature profile and average particle properties. The simulation was performed using the model parameters given Section 3. In Fig. 12(a) we see the rapid decomposition of TTIP as the temperature increases, accompanied by a spike in the concentration of $Ti(OH)_4$, the collision species. The $Ti(OH)_4$ concentration has two peaks, a consequence of the different speeds of the two reaction pathways in the chemical reaction model. The time evolution of average particle size, plotted in Fig. 12(b), follows a similar trajectory. An initial peak in particle size is observed corresponding to the first $Ti(OH)_4$ peak, which causes particle inception followed by growth through condensation and coalescence. A subsequent decrease in average primary size is

27

(a) Gas-phase species.　　　　(b) Particle properties.
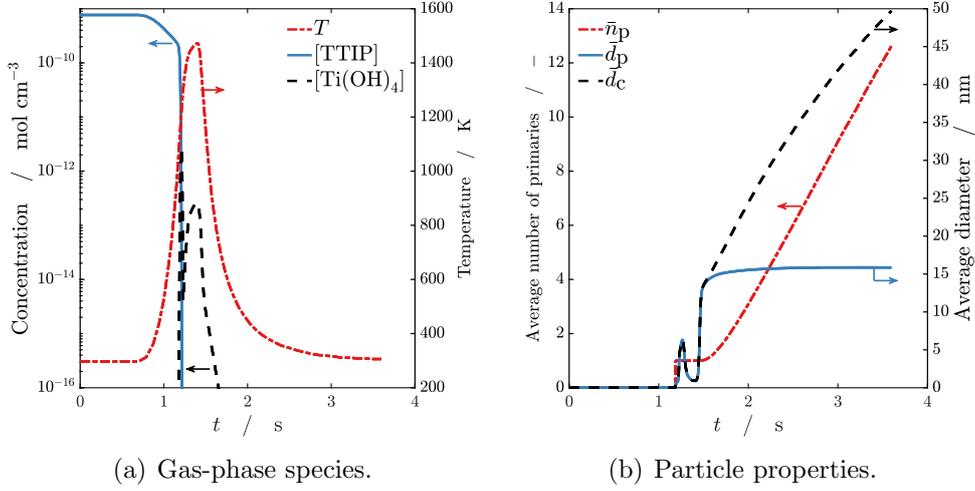
Figure 12: Time evolution of ((a)) key gas-phase species and imposed temperature profile, and ((b)) particle properties.

a consequence of the second peak in Ti(OH)$_4$ resulting in the inception of new small particles. In the high temperature region, the particles remain spherical due to their small size and the high sintering rate resulting in rapid coalescence of coagulating particles. Only once the temperature begins to decrease at $t \approx 1.5$ s we observe the beginning of aggregate formation. After this point, primary particle growth stops and aggregate growth proceeds via coagulation in the low temperature region of the reactor.

6.2. Sensitivity

In Fig. 13, we compare our detailed particle model simulations against the experimental and simulated aggregate and primary particle size distributions of Nakaso et al. [25, Fig. 9-2]. Our base case simulation results, using the parameters given in Section 3, are shown by the solid blue lines. Simulated primary particle diameters, $d_{p,i} = 2r_i$, are compared directly to the experimental primary diameters obtained from TEM measurements. The experimental aggregate mobility size measurements are compared to a modelled aggregate mobility diameter d_m for the free-molecular regime, estimated from the projected area A_{pr} [79]:

$$d_m = \sqrt{\frac{A_{pr}}{\pi}}. \tag{59}$$

Aggregate projected areas of 2048 randomly selected particles were obtained from image analysis, using the method described in [80], of projections produced using the algorithm given in Appendix B.6.

28

(a) Aggregate particle size distribution.　　(b) Primary particle size distribution.
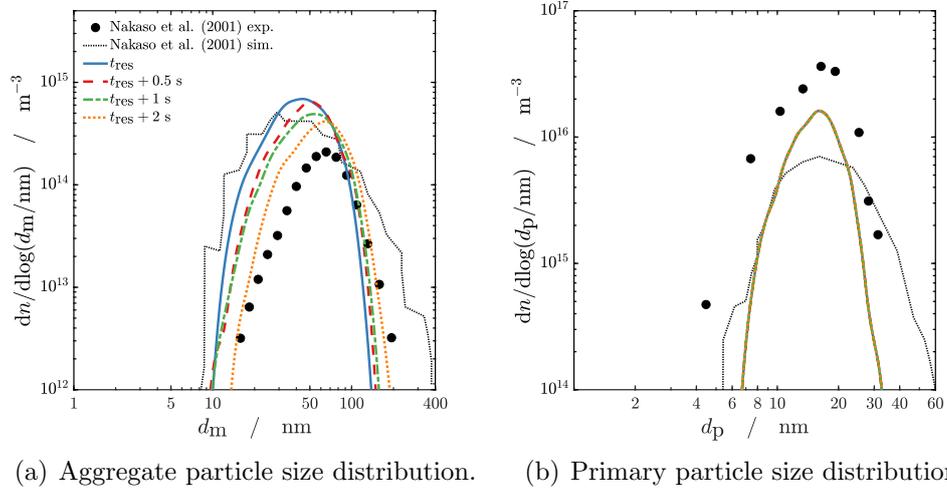
Figure 13: Aggregate and primary particle size distributions for the base case simulation (t_{res}) and for extended residence times ($t_{\mathrm{res}} + 0.5, 1, 2$ s). Note that the simulated primary PSDs (coloured lines) are all coincident. Experimental and simulation data from Nakaso et al. [25, Fig. 9-2] are included for comparison.

Our base case simulation underpredicts the peak of the aggregate PSD (Fig. 13(a)) while overpredicting the number density of aggregates. The predicted position of the peak in the primary PSD (Fig. 13(b)) is in excellent agreement with the experimental results of Nakaso et al. [25]; however, a narrower distribution and smaller primary number density are predicted.

Given the underprediction of aggregate size and overprediction of aggregate number density we consider extending the residence time to account for uncertainty arising from possible coagulation in the sampling lines at the end of reactor. Simulated TEM-style images produced using the method

(a) $t = t_{\mathrm{res}}$.　　(b) $t = t_{\mathrm{res}} + 2$ s.
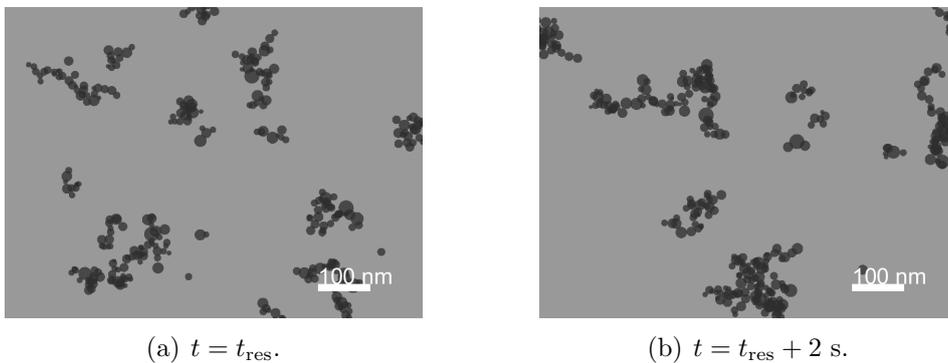
Figure 14: Simulated TEM-style images.

(a) Aggregate particle size distribution. (b) Primary particle size distribution.
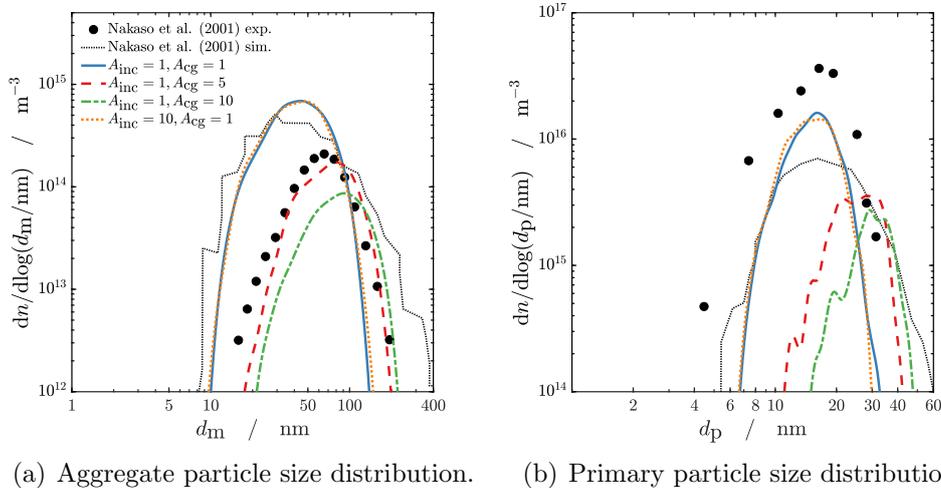
Figure 15: Sensitivity of simulated aggregate and primary particle size distributions to coagulation collision efficiency A_{cg} and inception collision efficiency A_{inc}. Experimental and simulation data from Nakaso et al. [25, Fig. 9-2] are included for comparison.

described in Appendix B.6 are presented in Fig. 14 for two cases: $t = t_{res}$ and $t = t_{res} + 2$ s. Qualitatively, the images show primary particles of similar size, but larger aggregates in the case with extended residence time. The primary and aggregate PSDs for $t_{res} + 0.5$ s, 1 s, 2 s are plotted in Fig. 13. The plots show that extending the residence time has no discernible effect on the primary PSD, but does shift the aggregate PSD to the right and reduce the number density towards the experimental data. However, to achieve agreement with the experimental PSD would require additional residence time of same order of magnitude as t_{res}, suggesting the system is relatively insensitive to possible uncertainty in the residence time.

In Fig. 15, we briefly look at the sensitivity of the aggregate and primary PSDs to the collision efficiency of coagulation and inception. The inception and coagulation rates are varied by introducing a multiplicative prefactor A_{inc} and A_{cg} to the respective kernels. Both the aggregate and primary PSDs are insensitive to an increase in the inception efficiency. Meanwhile, increasing the coagulation collision efficiency shifts both the aggregate and primary PSDs to the right and reduces the number density of aggregates and primary particles. The behaviour of the primary PSD is due to increased coalescence of coagulating primaries in the high temperature region of the reactor. A substantial increase in the coagulation efficiency improves the agreement in the aggregate PSD, but this is accompanied by a shift in the primary PSD away from the experimental data.

(a) Aggregate particle size distribution. (b) Primary particle size distribution.
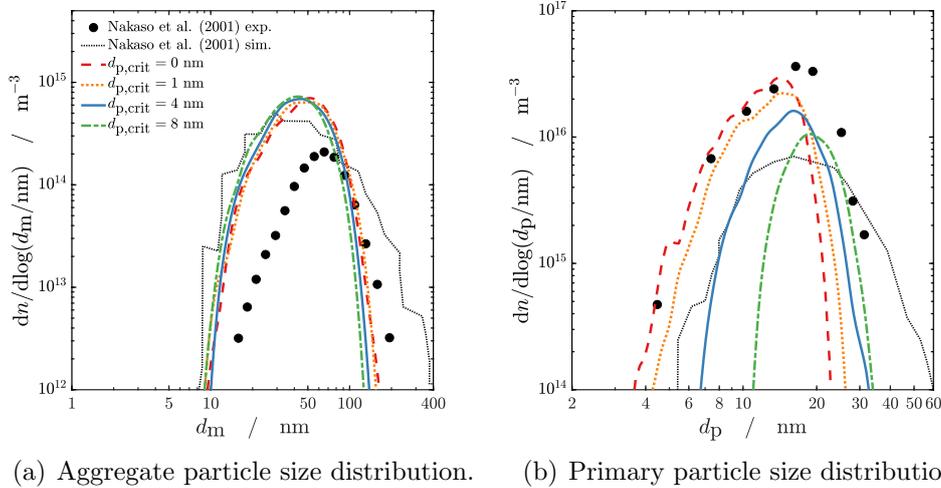
Figure 16: Sensitivity of simulated aggregate and primary particle size distributions to the critical sintering diameter $d_{\mathrm{p,crit}}$. Experimental and simulation data from Nakaso et al. [25, Fig. 9-2] are included for comparison.

The present coagulation model assumes ballistic aggregation of particles. However, near the end of the reactor the largest aggregates are in the transition regime ($\mathrm{Kn} \approx 1$), so collisions may in fact be diffusion limited. The effect of using a different aggregation model was investigated and simulations of the hot wall reactor with diffusion limited cluster aggregation (DLCA) showed no appreciable difference to the BCCA results.

Lastly, we look at the effect of the critical sintering diameter. Figure 16 shows the effect of varying $d_{\mathrm{p,crit}}$ on the aggregate and primary PSDs. The aggregate PSD is not very sensitive to the value of $d_{\mathrm{p,crit}}$, although a slight increase is observed with increasing $d_{\mathrm{p,crit}}$. The primary particle size distribution shows much greater sensitivity. For $d_{\mathrm{p,crit}} = 0$ nm we observe good agreement with the left hand tail of the experimental data while larger values shift the distribution towards the right hand tail of the experimental data. The best agreement in the position of the peak in the distribution is obtained for $d_{\mathrm{p,crit}} = 4$ nm. In all cases the number density of primaries is underpredicted.

In summary, the base case model parameters produced good agreement in the position of the primary PSD. However, the predicted width was narrower and primary number density was smaller. The position of the aggregate PSD was underpredicted, and the number denisty of aggregates overpredicted. The sensitivity of the aggregate and primary PSDs with respect to four parameters was investigated. The PSDs were relatively insensitive to

31

uncertainties in the residence time and insensitive to the collision efficiency of inception. Both the aggregate and primary size distribution were shown to be sensitive to the coagulation efficiency, while the critical sintering diameter was observed to only affect the primary PSD. The findings suggest that primary particle growth is driven by coagulation and sintering/coalescence in the high temperature region of the reactor with aggregate growth occurring in the subsequent low temperature region.

Given the observed sensitivity of the system to the coagulation and sintering processes a more extensive study should start by exploring the multi-dimensional parameter space for these processes in order to improve the model. Note that in the present work only one parameter was varied at a time, while the other parameters took their base case values. Moreover, the process rates could have additional dependencies that were not considered in the current work. For example, a recent study by Sharma et al. [81] showed that the coagulation efficiency of TiO_2 nanoparticles is strongly temperature dependent with significantly larger values at low temperature. This suggests that the coagulation rate may be underpredicted in the low temperature region of our simulations. If the rate was higher in this region, agreement in the aggregate PSD would be expected to improve while leaving the primary PSD unchanged. Furthermore, a molecular dynamics study on the sintering of nano-sized titania [74] suggests that the characteristic sintering time has a stronger dependence on the critical diameter than that used in the present work. This will be investigated in a future work.

7. Conclusions

We presented a new detailed particle model for titanium dioxide aggregates synthesised from TTIP precursor with inception, coagulation, condensation, sintering and coalescence. The new particle description resolves the radius, composition and position of each individual primary particle, representing an aggregate as a collection of overlapping spheres. The detailed geometrical description permits the morphological evolution of each aggregate to be simulated. The particle model developed in this work was presented in the context of titanium dioxide synthesised from TTIP precursor. However, the model can be easily adapted to wider applications such as different precursor chemistry (e.g. $TiCl_4$), materials (e.g. soot or silica) or particle process models (e.g. viscous flow sintering). Crucially, the model type space incorporates sufficient physical detail to relate particle processes to specific morphological transformations and provides a framework suitable for testing and discriminating between different process models.

The new particle model overcomes some of the limitations identified in previous models [6, 7] by adding more geometrical detail to the particle description; thereby permitting more physical detail to be incorporated into the process models. For example, a detailed description of the aggregate structure obtained by tracking individual primary coordinates allowed a more physical ballistic collision model to be implemented and avoided the need to assume fractal dimension in calculations. Most importantly, the detailed geometrical description allows for better comparison with experimental data. For instance, through visualisation of particles using TEM images that can be analysed in a similar manner to experimental TEMs (e.g. projected area) or by considering the effect of particle morphology on mobility measurements.

A numerical study was conducted using a simple batch reactor test case to investigate the convergence behaviour of a number of average properties. The study demonstrated that under conditions similar to the test case, convergence can be achieved in key properties for a feasible number of computational particles. Furthermore, the computational time for a converged solution was shown to be reasonable given an informed choice of operator splitting time step size.

Lastly, the hot wall reactor experiment of Nakaso et al. [25] was simulated. This was not intended to be a comprehensive evaluation of the model nor parameter fitting, but to briefly examine the model performance and make suggestions for future work. The base case model parameters produced reasonable agreement with the PSDs of Nakaso et al. [25], particularly the position of the peak of the primary size distribution. The simulated PSDs were shown to be sensitive to the coagulation efficiency and critical sintering diameter, suggesting that future work should investigate these process rates in more detail, paying particular attention to their size and temperature dependence. Next, it is important to further evaluate the model against experimental data and perform a thorough parametric sensitivity study.

Appendix A. Binary tree data structure

The primaries comprising an aggregate particle are stored in a binary tree data structure [6]. An example of a binary tree is shown in Fig. A.17.
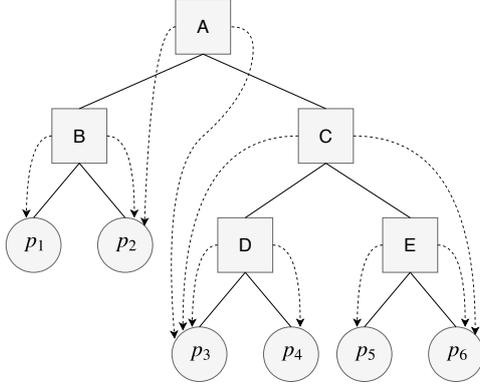
Figure A.17: Binary tree data structure.

The tree consists of a number of nodes where each node connects to two (child) nodes below it and a (parent) node above it – except for the top-most root node and bottom-most leaf nodes. These connections are shown by the solid lines in Fig. A.17. A leaf node (indicated by a circle) stores a single primary particle: in this case primaries $p_1...p_6$. A non-leaf node (squares labelled A...E) stores information pertaining to a single neck connecting two primaries. At the very least, this information should identify the two primaries connected by the neck. These connections are represented by the dashed lines in Fig. A.17. An important feature is that the two primaries must lie below their connecting node in the binary tree. For example, node C represents the neck connecting primaries p_3 and p_6. Node C could not, for instance, connect primary p_2 to p_3; this can only be achieved by a node above both primaries in the tree i.e. node A. The connectivity matrix representation for the binary tree structure is

$$
\mathbf{C} = \begin{pmatrix}
0 & & & \cdots & & 0 \\
1 & 0 & & & & \\
0 & 1 & 0 & & & \vdots \\
0 & 0 & 1 & 0 & & \\
0 & 0 & 0 & 0 & 0 & \\
0 & 0 & 1 & 0 & 1 & 0
\end{pmatrix}.
\tag{A.1}
$$

Figure A.18 shows two possible particle structures represented by the binary tree in Fig. A.17. The primaries are labelled $p_1...p_6$ and the necks are indicated by a red dot and labelled A...E. Since the binary tree only stores
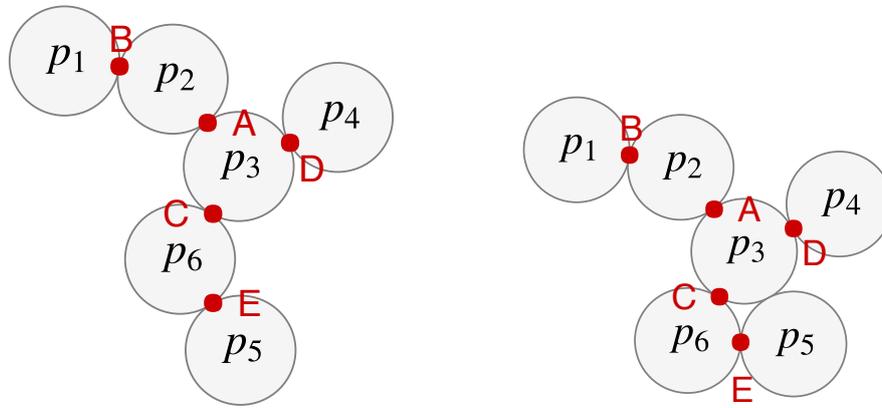
(a) Branched structure.

(b) Looped structure. Connectivity loop formed between primaries p_3, p_5 and p_6.

Figure A.18: Two different particle structures with the same binary tree connectivity – shown in Fig.A.17.

the connectivity and not the actual relative positions of primaries multiple particle structures are possible for a given binary tree. The actual positional information for each primary is stored in leaf node (primary) itself. This is fine for a branched structure such as that shown in Fig 18(a) but poses a problem for a looped structure such as the one shown in Fig. 18(b), where primary p_5 is in contact with p_3 but is not considered a neighbour. Such scenarios tend to occur when primaries, that were not initially in contact, sinter and grow producing a more compact structure with multiple overlaps such as shown in Fig. A.19.
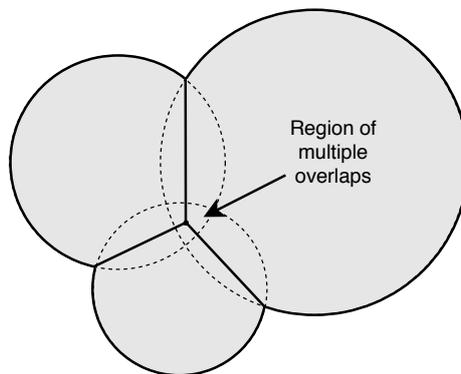
Figure A.19: Multiple overlapping primaries.

The consequence of a structure with multiple overlapping primaries is that the key model assumption – that necks are circular in cross section – no longer holds. This introduces inaccuracies into the the model equations e.g. calculation of the primary volume, free surface and neck area. To reduce the likelihood of this occurring, primaries can be merged sufficiently early to avoid large deviations from circular necks, but at point at which it is reasonable to approximate the sintered primaries as a single primary. This is handled by the coalescence process (Section 3.2.5). Another scenario in which looped structures arise is if two branches overlap. This cannot be avoided through primary coalescence, but the likelihood is reduced for less compact aggregates (small fractal dimensions).
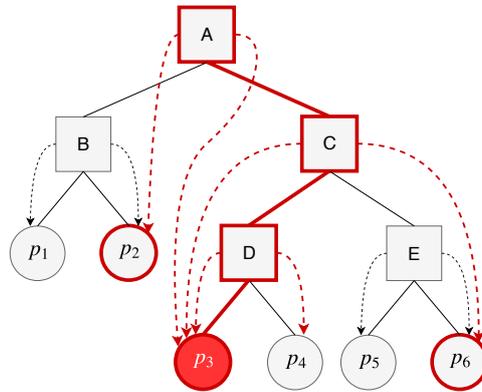
Figure A.20: Interrogating the binary tree for neighbours of p_3 by moving up the binary tree from the leaf node to root node along the path in bold red. The neighbours of p_3 and connections to non-leaf nodes are highlighted.

An important detail of the model equations is that they require summation over neighbours of a primary to calculate properties such as the primary volume, free surface and neck area etc. The binary tree provides a very efficient way to do this. Since each neck must be a non-leaf node located above the primary, it is only necessary to take a path from the primary of interest to the root node to find the neighbours; the rest of tree does not need to be explored. Figure A.20 shows an example of interrogating the binary tree for neighbours of p_3. The path taken is shown by the solid red bold lines along the route: p_3-D-C-A.

Appendix B. Algorithms

Appendix B.1. Direct simulation Monte-Carlo

The Direct Simulation Algorithm (DSA) is presented in Algorithm 1. Condensation and sintering are treated as deferred processes and performed using the Linear Process Deferment Algorithm (LPDA) [29]. The majorant kernel for coagulation and method of selecting particles is discussed by Patterson et al. [65]. Ensemble contractions and doublings are performed as discussed in Section 4.

Appendix B.2. Ballistic cluster-cluster aggregation

The implementation of ballistic cluster-cluster aggregation with a random impact parameter (BCCA) described by Jullien [57] is shown in Algorithm 2. Particle rotations are performed using the method proposed by Arvo [66] and particle bounding spheres are calculated using the method proposed by Ritter [67].

Test case. A test case is presented in the Supplementary Material.

Appendix B.3. Surface adjustment

A surface adjustment as a results of a condensation event is performed according to Algorithm 3. Note that we assume a primary is composed solely of discrete units of TiO_2. Therefore, a redistribution of composition (mass) between primaries only takes place if the volume change of the neighbour is sufficiently large. This can lead to some deviation between the volume derived from the composition

$$v_i = \frac{\eta_{TiO_2,i} M_{TiO_2}}{\rho_{TiO_2} N_A},$$ (B.1)

and the volume derived from the primary geometry

$$v_i = \frac{4}{3}\pi r_i^3 - \frac{1}{3}\pi \sum_j (2r_i^3 + x_{ij}^3 - 3r_i^2 x_{ij}).$$ (B.2)

The system, however, is to some extent self-correcting due to two processes. First, the movement of a neck during a surface adjustment will to a certain degree be offset by an opposing change during a possible future surface adjustment to the other primary. Second, the need to redistribute mass is eliminated by the merger of the two primaries during a coalescence event. Furthermore, the likelihood of the primaries coalescing is increased with more surface growth of one primary at the expense of the other.

Test case. A simple test case of constant growth is developed and compared to two limiting cases in the Supplementary Material.

Appendix B.4. Sintering

Sintering is performed on a particle P_q using Algorithm 4. Where two primaries are in point contact (i.e. their neck area is $A_{n,ij} = 0$) the sintering rate is undefined. In this case, we assume a neck radius of 1% of the smaller primary radius, $R_{ij} = \min(r_i, r_j)/100$.

Test case. A simple test case is presented and compared to a commonly employed excess surface area based sintering model in the Supplementary Material.

Appendix B.5. Coalescence

Neighbouring primaries p_i and p_j in a particle P_q are merged according to Algorithm 5, once the sintering level (Eq. (46)) exceeds $s_{ij} \geq 0.95$. The sintering level is defined while the neck remains between the primary particle centres and the primaries are merged as the neck leaves this region.

Appendix B.6. TEM images

A simulated TEM-style image is produced using Algorithm 6.

Algorithm 1: Direct simulation Monte-Carlo.

Input: State of system Q_0 at t_0; Final time t_f.
Output: State of system Q_f at t_f.
begin

    $Q \leftarrow Q_0$;
    $t \leftarrow t_0$;
    while $t < t_\mathrm{f}$ **do**

        Calculate total rate of non-deferred processes:

$$R_\mathrm{tot}(Q) = \sum_m R_m(Q),$$

        with $m \in \{\mathrm{inc}, \mathrm{cg}\}$ and where $R_\mathrm{cg} = \hat{R}_\mathrm{cg}(Q)$;
        Calculate an exponentially distributed waiting time:

$$\tau = -\frac{\ln U}{R_\mathrm{tot}},$$

        where U is a uniformly distributed random variable, $U \in [0, 1]$;

        Select a process with probability:

$$P(m) = \frac{R_m(Q)}{R_\mathrm{tot}(Q)};$$

        if $m = \mathrm{inc}$ **then**
            `/* This is an inception event            */`
            Create a new particle P_N and add it to the ensemble;
            if $N > N_\mathrm{max}$ **then**
                Uniformly remove a particle;
                Contract ensemble;

        else
            `/* This is a coagulation event           */`
            Select two particles P_q and P_r;
            Calculate majorant for two particles: $\hat{K}_\mathrm{cg}^\mathrm{tr}(P_q, P_r)$;
            Perform deferred processes for P_q and P_r (condensation
             and sintering);
            Calculate true kernel for the two particles: $K_\mathrm{cg}^\mathrm{tr}(P_q, P_r)$;
            With probability

$$P = \frac{K_\mathrm{cg}^\mathrm{tr}(P_q, P_r)}{\hat{K}_\mathrm{cg}^\mathrm{tr}(P_q, P_r)},$$

            perform BCCA coagulation: $P_q + P_r \rightarrow P_s$;
            if $N < N_\mathrm{max}/2$ **then**
                Double the ensemble;

        $t \leftarrow t + \tau$;

    Perform deferred processes (condensation and sintering) for all
     particles;
    return Q

Algorithm 2: Ballistic cluster-cluster algorithm with a random impact parameter.

Input: Particles P_q and P_r chosen for coagulation.

Output: Daughter particle P_s.

begin

    Randomly rotate P_q and P_r around their centres of mass (using Ref. [66])

    Calculate the bounding spheres $r_b(P_q)$ and $r_b(P_r)$ (using Ref. [67])

    Centre the bounding spheres

    repeat

        `/* Determine random trajectory                */`

        Uniformly select a point $H_1(\theta, \phi)$ on a unit sphere:

$$\phi = 2\pi U \quad \text{and} \quad \theta = \arccos(2U - 1),$$

        where U is a uniformly distributed random variable;

        Construct a rotation matrix $\mathbf{R}$ that rotates the vector $(0, 0, -1)$ to the point H_1;

        `/* Determine random impact parameter          */`

        Uniformly select a point:

$$H_2 = (R\sqrt{r}\cos\theta, R\sqrt{r}\sin\theta, -R),$$

        on a disk of radius $R = r_b(P_q) + r_b(P_r)$ centred on $(0,0,-R)$ in the $z = -R$ plane with $r = U$, and $\theta = 2\pi U$, where U is a uniformly distributed random variable;

        `/* Set initial positions                      */`

        Apply the rotation to H_2 giving a new point $H_3 = \mathbf{R}H_2$;

        Place particle P_r at point H_3;

        Place particle P_q at $O = (0, 0, 0)$;

        `/* Perform the collision                      */`

        while *No point of contact* **do**

            Translate P_r along a vector parallel to $H_1 O$ by distance $R/100$;

            Check for contact;

            if *P_r has passed through the bounding sphere of P_q* **then**

                `/* This is an unsuccessful collision      */`

                Break;

        if *Single point of contact* **then**

            `/* This is a successful collision          */`

            New particle P_s created by connecting the binary trees of P_q and P_r at a new head node;

            Contacting primaries p_i and p_j connected at the new head node;

            return *New particle P_s*

    until *Successful collision*

Algorithm 3: Surface growth

Input: Particle P_q; Number of units of TiO$_2$ added $\Delta\eta$
Output: Particle P_q
begin

    Select a primary p_i in particle P_q with probability

$$P(p_i) = \frac{A_i}{\sum_{j=1}^{n_{\mathrm{p}}(P_q)} A_j};$$

    Save old volume and radius: $v_{i,\mathrm{old}} \leftarrow v_i$ and $r_{i,\mathrm{old}} \leftarrow r_i$;
    Update primary composition: $\eta_i \leftarrow \eta_i + \Delta\eta$;
    Calculate new volume, v_i;
    while $v_{i,\mathrm{old}} < v_i$ **do**

        `/* Primary radius increased in 1% increments    */`
        $\Delta r \leftarrow r_i/100$;
        $\Delta v \leftarrow A_i \Delta r$;
        if $v_{i,old} + \Delta v > v_i$ **then**

$$\Delta r \leftarrow \frac{(v_i - v_{i,\mathrm{old}})}{\Delta v}\Delta r;$$

        Increase radius: $r_i \leftarrow r_i + \Delta r$;
        Update free surface area, A_i;
        $v_{i,\mathrm{old}} \leftarrow v_{i,\mathrm{old}} + \Delta v$;

    `/* Redistribution of composition between neighbours  */`
    foreach Neighbour p_j of p_i **do**

        Estimate change in volume of p_j:

$$\Delta v_j \leftarrow -A_{\mathrm{n},ij}\frac{r_{i,\mathrm{old}}}{d_{ij}}\left(r_i - r_{i,\mathrm{old}}\right);$$

        Calculate (integer) change in composition of p_j:

$$\Delta\eta_j \leftarrow \frac{\Delta v_j}{M_{\mathrm{TiO}_2}/\left(\rho_{\mathrm{TiO}_2}N_{\mathrm{A}}\right)},$$

        rounded down to the nearest integer;
        if $|\Delta\eta_j| > 0$ **then**
            Update the composition of p_j: $\eta_j \leftarrow \eta_j + \Delta\eta_j$;
            Update the composition of p_i: $\eta_i \leftarrow \eta_i - \Delta\eta_j$;

    return P_q

Algorithm 4: Sintering

Input: Particle P_q; Time to sinter particle t_{sint}
Output: Particle P_q
begin
    foreach *Neck between two primaries p_i and p_j in particle P_q* **do**
        $\Delta d_{ij,\text{max}} \leftarrow d_{ij}/100$;
        $t \leftarrow 0$;
        while $t < t_{\text{sint}}$ **do**
            Calculate sintering rate: $\frac{\mathrm{d}d_{ij}}{\mathrm{d}t}$ (Eq. (35));
            Calculate time step:

$$\Delta t \leftarrow \frac{\Delta d_{ij,\text{max}}}{\frac{\mathrm{d}d_{ij}}{\mathrm{d}t}};$$

            if $t_{\text{sint}} > t + \Delta t$ **then**

$$\mu \leftarrow 100;$$

            else

$$\mu \leftarrow 100\frac{(t_{\text{sint}} - t)}{\Delta d_{ij,\text{max}}}\frac{\mathrm{d}d_{ij}}{\mathrm{d}t};$$

            Generate a Poisson random variate X with mean μ;
            Calculate change in separation:

$$\Delta d_{ij} = -\frac{X}{100}\Delta d_{ij,\text{max}};$$
$$\Delta \mathbf{d}_{ij} = -\Delta d_{ij}\frac{\mathbf{x}_j - \mathbf{x}_i}{|\mathbf{x}_j - \mathbf{x}_i|};$$

            Adjust centre to centre separation: $d_{ij} \leftarrow d_{ij} + \Delta d_{ij}$;
            `/* Only need to adjust the coordinates of`
               `primaries on one side of the neck, in this`
               `case` p_i.   `*/`
            Translate primary p_i: $\mathbf{x}_i \leftarrow \mathbf{x}_i + \Delta \mathbf{d}_{ij}$;
            `Translate neighbours` $(p_i; p_j; \Delta \mathbf{d}_{ij})$;
            Compute change in radii using Eq. (45): Δr_i and Δr_j;
            `Adjust connectivity` $(p_i; p_j; \Delta r_i)$;
            `Adjust connectivity` $(p_j; p_i; \Delta r_j)$;
            Update primary radii:

$$r_i \leftarrow r_i + \Delta r_i$$
$$r_j \leftarrow r_j + \Delta r_j$$

            Update properties of primaries p_i and p_j;
            $t \leftarrow t + \Delta t$;
            if *Coalescence condition is met* **then**
               Merge primaries p_i and p_j;
               Break;

Algorithm 4: Sintering Cont.

```
/* Translates all the neighbours of a primary p_i by Δd_ij,
   except for neighbour p_j                                    */
```
Function Translate neighbours (Primary p_i; Neighbour p_j;
 Translation $\Delta\mathbf{d}$)

    foreach *Neighbour p_k of p_i, except for primary p_j* **do**

        Translate p_k by $\Delta\mathbf{d}$;

$$\mathbf{x}_k \leftarrow \mathbf{x}_k + \Delta\mathbf{d};$$

```
      /* Recursively translate the neighbours of p_k,
         except for primary p_i                                */
```
        Translate neighbours (Primary p_k; Neighbour p_i;
         Translation $\Delta\mathbf{d}$);

```
/* Update centre to centre separations and coordinates of
   neighbours p_k of primary p_i except for neighbour p_j   */
```
Function Adjust connectivity (Primary p_i; Neighbour p_j; Δr_i)

    foreach *Neck between primary p_i and neighbour p_k, except for primary p_j* **do**

        Calculate change in separation (Eq. (40)):

$$\Delta d_{ik} = \frac{r_i}{x_{ik}}\Delta r_i;$$
$$\Delta\mathbf{d}_{ik} = \Delta d_{ik}\frac{\mathbf{x}_k - \mathbf{x}_i}{|\mathbf{x}_k - \mathbf{x}_i|};$$

        Translate neighbour to update centre to centre separation:

$$d_{ik} \leftarrow d_{ik} + \Delta d_{ik};$$
$$\mathbf{x}_k \leftarrow \mathbf{x}_k + \Delta\mathbf{d}_{ik};$$

        Translate neighbours (Primary p_k; Neighbour p_i;
         Translation $\Delta\mathbf{d}_{ik}$);

Algorithm 5: Merger

Input: Particle P_q; Primaries p_i and p_j to merge

Output: Particle P_q with merged primary $p_{i,\text{new}}$

```
/* We assume that p_i is the larger primary:   r_i > r_j        */
```

begin

    Solve Eq. (48) for the new merge primary radius of $r_{i,\text{new}}$;

    Update the composition of p_i: $\eta_{i,\text{new}} = \eta_i + \eta_j$;

    foreach *Neck between p_i and neighbour p_k except p_j* **do**

$$x_{ki} = \frac{d_{ik}^2 - r_i^2 + r_k^2}{2d_{ik}};$$

$$\Delta d_{ik} = \max\left(x_{ki} \pm \sqrt{x_{ki}^2 - r_k^2 + r_{i,\text{new}}}\right) - d_{ik};$$

$$\Delta \mathbf{d}_{ik} = \Delta d_{ik}\frac{\mathbf{x}_k - \mathbf{x}_i}{|\mathbf{x}_k - \mathbf{x}_i|};$$

        Translate neighbour p_k:

$$d_{ik} \leftarrow d_{ik} + \Delta d_{ik};$$

$$\mathbf{x}_k \leftarrow \mathbf{x}_k + \Delta \mathbf{d}_{ik};$$

        `Translate neighbours` (Primary p_k; Neighbour p_i; Translation $\Delta \mathbf{d}_{ik}$);

```
/* The function Translate neighbours is defined in
   Algorithm  4                                    */
```

    foreach *Neck between p_j and neighbour p_l except p_i* **do**

$$x_{lj} = \frac{d_{jl}^2 - r_j^2 + r_k^2}{2d_{jl}};$$

$$\Delta d_{il} = \max\left(x_{lj} \pm \sqrt{x_{lj}^2 - r_l^2 + r_{i,\text{new}}}\right) - d_{il};$$

$$\Delta \mathbf{d}_{il} = \Delta d_{il}\frac{\mathbf{x}_l - \mathbf{x}_i}{|\mathbf{x}_l - \mathbf{x}_i|};$$

        Translate neighbour p_l:

$$d_{il} \leftarrow d_{il} + \Delta d_{il};$$

$$\mathbf{x}_l \leftarrow \mathbf{x}_l + \Delta \mathbf{d}_{il};$$

        `Translate neighbours` (Primary p_l; Neighbour p_j; Translation $\Delta \mathbf{d}_{il}$);

    $r_i \leftarrow r_{i,\text{new}}$;

    Remove primary p_j and restructure binary tree ;

    Update particle properties;

    return P_q

Algorithm 6: TEM images

Input: Ensemble Q; Frame size $2a \times 2b$; Particles per frame N;
        Number of images n

Output: n TEM images

begin
    for *n frames* **do**
        for *N particles* **do**
            Uniformly select a particle P_q from ensemble Q;
            Randomly rotate P_q around its centres of mass using the
              method descibed by Arvo [66];
            Generate (x, y) coordinates uniformly in the image plane
              with $-a \leq x \leq a$ and $-b \leq y \leq b$;
            Position P_q in the image plane with its centre of mass at
              (x, y);
            Project P_q into the image plane;
            Remove P_q from the ensemble;

Nomenclature

Upper-case Roman

A	Surface area
$A_{\text{inc/cg}}$	Inception/coagulation rate prefactor
B	Auxiliary sintering variable
$\mathbf{C}$	Aggregate particle connectivity matrix
C_{v0}	Equilibrium vacancy concentration
C_{ij}	Connectivity matrix element
D_{f}	Fractal dimension
D_{v}	Vacancy diffusion coefficient
F_v	Volume fraction
$H_{1/2/3}$	Coordinates
I_P	Confidence interval
K	Collision kernel
$\hat{K}$	Majorant collision kernel
Kn	Knudsen number
L	Number of runs
M_0	Zeroth moment/Aggregate particle number density
M	Molar mass
M	Total number of time steps
N	Number of aggregate/computational particles
N_{A}	Avogadro constant
O	Origin coordinates
P	Probability
P_q	Aggregate particle
Q	State of system
$\mathbf{R}$	Rotation matrix
R	Radius
R	Rate
$\hat{R}$	Majorant rate
R_{ij}	Neck radius
T	Temperature
U	Uniformly distributed random variable
V	Volume
X	Poisson distributed random variable

Lower-case Roman

a_P	Critical value of the standard normal distribution for confidence level P
c_P	Half-width of the confidence interval
d	Diameter
$\bar{d}$	Population average diameter
d_{ij}	Centre to centre separation of primaries p_i and p_j
e_{r}	Relative error
e_{tot}	Total relative error
k_{f}	Fractal pre-factor
k_{B}	Boltzmann constant
m	Mass
n_{p}	Number of primaries
$\bar{n}_{\mathrm{p}}$	Population average number of primaries
p	Pressure
p_i	Primary particle
r	Radius
s	Sintering level
$\bar{s}$	Population average sintering level
t	Time
v	Volume (primary particle)
$\mathbf{x}_i$	Position vector of the centre of primary p_i
x_{ij}	Distance from the centre of primary p_i to the neck with p_j

Upper-case Greek

Ω	Vacancy volume

Lower-case Greek

γ	Surface free energy
δ_{gb}	Grain boundary thickness
ϵ	Collision enhancement factor
ζ	High precision solution to general macroscopic quantity of system
η	Primary composition: number of chemical units
θ	Polar angle
λ	Mean free path

μ	Gas-phase viscosity
μ	Mean
μ_1	Mean
μ_2	Variance
ξ_l	General macroscopic quantity of system measured for run l
ρ	Density
τ	Exponentially distributed waiting time
ϕ	Azimuthal angle

Superscripts

const	Denotes a constant kernel
fm	Denotes the free molecular regime
sf	Denotes the slip flow regime
tr	Denotes the transition regime

Subscripts

0	Denotes an initial value
agg	Denotes an aggregate property
avg	Denotes the particle average value
b	Bounding sphere
c	Collision
cap	Spherical cap
cg	Coagulation
cond	Condensation
crit	Denotes the critical sintering diameter
sph	Sphere
f	Denotes a final value
g	Gyration
gp	Denotes the radius of gyration of a spherical primary particle
$i/j/k/l/m$	Primary particle index
inc	Inception
j	Time step index
l	Simulation run index
m	Particle process index
m	Mobility
max	Maximum

n	Denotes the neck
p	Primary particle
pr	Projected
$q/r/s$	Aggregate particle index
res	Denotes the reactor residence time
s	Denotes a splitting step
sint	Sintering
smpl	Sample
tot	Total

Abbreviations

BCCA	Ballistic Cluster Cluster Aggregation
CPU	Central Processing Unit
DEM	Discrete Element Method
DSA	Direct Simulation Algorithm
LPDA	Linear Process Deferment Algorithm
ODE	Ordinary Differential Equation
PBM	Population Balance Model
PSD	Particle Size Distribution
TEM	Transmission Electron Microscopy
TTIP	Titanium Tetraisopropoxide

References

[1] W. J. Menz, M. Kraft, The suitability of particle models in capturing aggregate structure and polydispersity, Aerosol Sci. Technol. 47 (2013) 734–745, doi:10.1080/02786826.2013.788244.

[2] M. Frenklach, S. J. Harris, Aerosol dynamics modeling using the method of moments, J. Colloid Interface Sci. 118 (1987) 252–261, doi: 10.1016/0021-9797(87)90454-1.

[3] Y. Xiong, S. E. Pratsinis, Formation of agglomerate particles by coagulation and sintering–Part I. A two-dimensional solution of the population balance equation, J. Aerosol Sci. 24 (1993) 283–300, doi:10.1016/0021-8502(93)90003-R.

[4] F. E. Kruis, K. A. Kusters, S. E. Pratsinis, B. Scarlett, A simple model for the evolution of the characteristics of aggregate particles undergoing coagulation and sintering, Aerosol Sci. Technol. 19 (1993) 514–526, doi: 10.1080/02786829308959656.

[5] M. C. Heine, S. E. Pratsinis, Polydispersity of primary particles in agglomerates made by coagulation and sintering, J. Aerosol Sci. 38 (2007) 17–38, doi:10.1016/j.jaerosci.2006.09.005.

[6] M. Sander, R. H. West, M. S. Celnik, M. Kraft, A detailed model for the sintering of polydispersed nanoparticle agglomerates, Aerosol Sci. Technol. 43 (2009) 978–989, doi:10.1080/02786820903092416.

[7] S. Shekar, W. J. Menz, A. J. Smith, M. Kraft, W. Wagner, On a multivariate population balance model to describe the structure and composition of silica nanoparticles, Comput. Chem. Eng. 43 (2012) 130–147, doi:10.1016/j.compchemeng.2012.04.010.

[8] D. Chen, Z. Zainuddin, E. Yapp, J. Akroyd, S. Mosbach, M. Kraft, A fully coupled simulation of PAH and soot growth with a population balance model, Proc. Combust. Inst. 34 (2013) 1827–1835, doi:10.1016/j.proci.2012.06.089.

[9] P. Mitchell, M. Frenklach, Monte carlo simulation of soot aggregation with simultaneous surface growth-why primary particles appear spherical, Symp. (Int.) Combust. 27 (1998) 1507–1514, doi:10.1016/S0082-0784(98)80558-4.

[10] P. Mitchell, M. Frenklach, Particle aggregation with simultaneous surface growth, Phys. Rev. E 67 (2003) 061407, doi:10.1103/PhysRevE.67.061407.

[11] N. Morgan, M. Kraft, M. Balthasar, D. Wong, M. Frenklach, P. Mitchell, Numerical simulations of soot aggregation in premixed laminar flames, Proc. Combust. Inst. 31 (2007) 693–700, doi:10.1016/j.proci.2006.08.021.

[12] M. L. Eggersdorfer, D. Kadau, H. J. Herrmann, S. E. Pratsinis, Multiparticle sintering dynamics: From fractal-like aggregates to compact structures, Langmuir 27 (2011) 6358–6367, doi:10.1021/la200546g.

[13] R. Mcgraw, Description of Aerosol Dynamics by the Quadrature Method of Moments, Aerosol Sci. Technol. 27 (1997) 255–265, doi:10.1080/02786829708965471.

[14] J. I. Jeong, M. Choi, A bimodal moment model for the simulation of particle growth, J. Aerosol Sci. 35 (2004) 1071–1090, doi:10.1016/j.jaerosci.2004.04.005.

[15] Y. Sung, V. Raman, H. Koo, M. Mehta, R. O. Fox, Large-eddy simulation modeling of turbulent flame synthesis of titania nanoparticles using a bivariate particle description, AIChE J. 60 (2014) 459–472, doi:10.1002/aic.14279.

[16] D. L. Wright, R. McGraw, D. E. Rosner, Bivariate extension of the quadrature method of moments for modeling simultaneous coagulation and sintering of particle populations, J. Colloid Interface Sci. 236 (2001) 242–251, doi:10.1006/jcis.2000.7409.

[17] D. L. Marchisio, R. O. Fox, Solution of population balance equations using the direct quadrature method of moments, J. Aerosol Sci. 36 (2005) 43–73, doi:10.1016/j.jaerosci.2004.07.009.

[18] M. E. Mueller, G. Blanquart, H. Pitsch, A joint volume-surface model of soot aggregation with the method of moments, Proc. Combust. Inst. 32 (2009) 785–792, doi:10.1016/j.proci.2008.06.207.

[19] M. E. Mueller, G. Blanquart, H. Pitsch, Hybrid Method of Moments for modeling soot formation and growth, Combust. Flame 156 (2009) 1143–1155, doi:10.1016/j.combustflame.2009.01.025.

[20] F. Gelbard, Y. Tambour, J. H. Seinfeld, Sectional Representations for Simulating Aerosol Dynamics, J. Colloid Interface Sci. 76 (1980) 541–556.

[21] J. J. Wu, R. C. Flagan, A Discrete-Sectional Solution to the Aerosol Dynamic Equation, J. Colloid Interface Sci. 123 (1988) 339–352.

[22] P. T. Spicer, O. Chaoul, S. Tsantilis, S. E. Pratsinis, Titania formation by $TiCl_4$ gas phase oxidation, surface growth and coagulation, J. Aerosol Sci. 33 (2002) 17–34, doi:10.1016/S0021-8502(01)00069-6.

[23] S. Tsantilis, H. K. Kammler, S. E. Pratsinis, Population balance modeling of flame synthesis of titania nanoparticles, Chem. Eng. Sci. 57 (2002) 2139–2156, doi:10.1016/S0009-2509(02)00107-0.

[24] J. I. Jeong, M. Choi, A sectional method for the analysis of growth of polydisperse non-spherical particles undergoing coagulation and coalescence, J. Aerosol Sci. 32 (2001) 565–582, doi:10.1016/S0021-8502(00)00103-8.

[25] K. Nakaso, T. Fujimoto, T. Seto, M. Shimada, K. Okuyama, M. M. Lunden, Size distribution change of titania nano-particle agglomerates

generated by gas phase reaction, agglomeration, and sintering, Aerosol Sci. Technol. 35 (2001) 929–947, doi:10.1080/02786820126857.

[26] A. Eibeck, W. Wagner, An efficient stochastic algorithm for studying coagulation dynamics and gelation phenomena, SIAM J. Sci. Comput. 22 (2000) 802–821, doi:10.1137/S1064827599353488.

[27] M. Goodson, M. Kraft, An efficient stochastic algorithm for simulating nano-particle dynamics, J. Comput. Phys. 183 (2002) 210–232, doi:10.1006/jcph.2002.7192.

[28] N. M. Morgan, C. G. Wells, M. J. Goodson, M. Kraft, W. Wagner, A new numerical approach for the simulation of the growth of inorganic nanoparticles, J. Comput. Phys. 211 (2006) 638–658, doi:10.1016/j.jcp.2005.04.027.

[29] R. I. A. Patterson, J. Singh, M. Balthasar, M. Kraft, J. R. Norris, The linear process deferment algorithm: A new technique for solving population balance equations, SIAM J. Sci. Comput. 28 (2006) 303–320, doi:10.1137/040618953.

[30] H. Zhao, F. E. Kruis, C. Zheng, A differentially weighted Monte Carlo method for two-component coagulation, J. Comput. Phys. 229 (2010) 6931–6945, doi:10.1016/j.jcp.2010.05.031.

[31] J. Singh, M. Balthasar, M. Kraft, W. Wagner, Stochastic modeling of soot particle size and age distributions in laminar premixed flames, Proc. Combust. Inst. 30 (2005) 1457–1464, doi:10.1016/j.proci.2004.08.120.

[32] E. K. Y. Yapp, R. I. A. Patterson, J. Akroyd, S. Mosbach, E. M. Adkins, J. H. Miller, M. Kraft, Numerical simulation and parametric sensitivity study of optical band gap in a laminar co-flow ethylene diffusion flame, Combust. Flame 167 (2016) 320 – 334, doi:10.1016/j.combustflame.2016.01.033.

[33] C. S. Lindberg, M. Y. Manuputty, J. Akroyd, M. Kraft, A two-step simulation methodology for modelling stagnation flame synthesised aggregate nanoparticles, Combust. Flame 202 (2019) 143–153, doi:10.1016/j.combustflame.2019.01.010.

[34] D. Hou, C. S. Lindberg, M. Y. Manuputty, X. You, M. Kraft, Modelling soot formation in a benchmark ethylene stagnation flame with a new detailed population balance model, Combust. Flame 203 (2019) 56–71, doi:10.1016/j.combustflame.2019.01.035.

[35] A. Boje, J. Akroyd, S. Sutcliffe, J. Edwards, M. Kraft, Detailed population balance modelling of TiO_2 synthesis in an industrial reactor, Chem. Eng. Sci. 164 (2017) 219–231, doi:10.1016/j.ces.2017.02.019.

[36] W. J. Menz, J. Akroyd, M. Kraft, Stochastic solution of population balance equations for reactor networks, J. Comput. Phys. 256 (2014) 615–629, doi:10.1016/j.jcp.2013.09.021.

[37] R. Irizarry, Fast compartmental Monte Carlo simulation of population balance models: application to nanoparticle formation in nonhomogeneous conditions, Ind. Eng. Chem. Res. 51 (2012) 15484–15496, doi: 10.1021/ie3011116.

[38] F. E. Kruis, J. Wei, T. van der Zwaag, S. Haep, Computational fluid dynamics based stochastic aerosol modeling: combination of a cell-based weighted random walk method and a constant-number Monte-Carlo method for aerosol dynamics, Chem. Eng. Sci. 70 (2012) 109–120, doi: 10.1016/j.ces.2011.10.040.

[39] H. Zhao, C. Zheng, A population balance-Monte Carlo method for particle coagulation in spatially inhomogeneous systems, Comput. Fluids 71 (2013) 196–207, doi:10.1016/j.compfluid.2012.09.025.

[40] M. L. Eggersdorfer, D. Kadau, H. J. Herrmann, S. E. Pratsinis, Aggregate morphology evolution by sintering: Number and diameter of primary particles, J. Aerosol Sci. 46 (2012) 7–19, doi: 10.1016/j.jaerosci.2011.11.005.

[41] E. Goudeli, M. L. Eggersdorfer, S. E. Pratsinis, Coagulation-agglomeration of fractal-like particles: Structure and self-preserving size distribution, Langmuir 31 (2015) 1320–1327, doi:10.1021/la504296z.

[42] E. Goudeli, M. L. Eggersdorfer, S. E. Pratsinis, Coagulation of agglomerates consisting of polydisperse primary particles, Langmuir 32 (2016) 9276–9285, doi:10.1021/acs.langmuir.6b02455.

[43] G. A. Kelesidis, E. Goudeli, S. E. Pratsinis, Flame synthesis of functional nanostructured materials and devices: Surface growth and aggregation, Proc. Combust. Instit. 36 (2017) 29–50, doi:10.1016/j.proci.2016.08.078.

[44] G. A. Kelesidis, E. Goudeli, S. E. Pratsinis, Morphology and mobility diameter of carbonaceous aerosols during agglomeration and surface growth, Carbon 121 (2017) 527–535, doi:10.1016/j.carbon.2017.06.004.

[45] H. J. Schmid, S. Tejwani, C. Artelt, W. Peukert, Monte Carlo simulation of aggregate morphology for simultaneous coagulation and sintering, J. Nanoparticle Res. 6 (2004) 613–626, doi:10.1007/s11051-004-2161-x.

[46] P. Lavvas, M. Sander, M. Kraft, H. Imanaka, Surface chemistry and particle shape: Processes for the evolution of aerosols in Titan's atmosphere, Astrophys. J. 728 (2011) 80, doi:10.1088/0004-637X/728/2/80.

[47] M. Celnik, A. Raj, R. West, R. Patterson, M. Kraft, Aromatic site description of soot particles, Combust. Flame 155 (2008) 161–180, doi: 10.1016/j.combustflame.2008.04.011.

[48] M. S. Celnik, M. Sander, A. Raj, R. H. West, M. Kraft, Modelling soot formation in a premixed flame using an aromatic-site soot model and an improved oxidation rate, Proc. Combust. Inst. 32 (2009) 639–646, doi:10.1016/j.proci.2008.06.062.

[49] C. G. Wells, N. M. Morgan, M. Kraft, W. Wagner, A new method for calculating the diameters of partially-sintered nanoparticles and its effect on simulated particle properties, Chem. Eng. Sci. 61 (2006) 158–166, doi:10.1016/j.ces.2005.01.048.

[50] N. M. Morgan, R. I. A. Patterson, M. Kraft, Modes of neck growth in nanoparticle aggregates, Combust. Flame 152 (2008) 272–275, doi: 10.1016/j.combustflame.2007.08.007.

[51] M. Sander, R. I. A. Patterson, A. Braumann, A. Raj, M. Kraft, Developing the PAH-PP soot particle model using process informatics and uncertainty propagation, Proc. Combust. Inst. 33 (2011) 675–683, doi: 10.1016/j.proci.2010.06.156.

[52] M. Zurita-Gotor, D. E. Rosner, Effective diameters for collisions of fractal-like aggregates: Recommendations for improved aerosol coagulation frequency predictions, J. Colloid Interface Sci. 255 (2002) 10–26, doi:10.1006/jcis.2002.8634.

[53] C. M. Sorensen, The mobility of fractal aggregates: A review, Aerosol Sci. Technol. 45 (2011) 765–779, doi:10.1080/02786826.2011.560909.

[54] M. L. Eggersdorfer, S. E. Pratsinis, Agglomerates and aggregates of nanoparticles made in the gas phase, Adv. Powder Technol. 25 (2014) 71–90, doi:10.1016/j.apt.2013.10.010.

[55] A. V. Filippov, M. Zurita, D. E. Rosner, Fractal-like aggregates: Relation between morphology and physical properties, J. Colloid Interface Sci. 229 (2000) 261–273, doi:10.1006/jcis.2000.7027.

[56] C. Lindberg, J. Akroyd, M. Kraft, Developing breakage models relating morphological data to the milling behaviour of flame synthesised titania particles, Chem. Eng. Sci. 166 (2017) 53–65, doi:10.1016/j.ces.2017.03.016.

[57] R. Jullien, Transparency effects in cluster-cluster aggregation with linear trajectories, J. Phys. A: Math. Gen. 17 (1984) L771–L776, doi:10.1088/0305-4470/17/14/009.

[58] H. Wang, X. You, A. V. Joshi, S. G. Davis, A. Laskin, F. Egolfopoulos, C. K. Law, USC mech version II. High-temperature combustion reaction model of $H_2/CO/C_1$-C_4 compounds, URL `http://ignis.usc.edu/USC_Mech_II.htm`, accessed on 12 December 2015, 2007.

[59] P. Buerger, D. Nurkowski, J. Akroyd, M. Kraft, A kinetic mechanism for the thermal decomposition of titanium tetraisopropoxide, Proc. Combust. Inst. 36 (2017) 1019–1027, doi:10.1016/j.proci.2016.08.062.

[60] P. Buerger, D. Nurkowski, J. Akroyd, S. Mosbach, M. Kraft, First-principles thermochemistry for the thermal decomposition of titanium tetraisopropoxide, J. Phys. Chem. A 119 (2015) 8376–8387, doi:10.1021/acs.jpca.5b01721.

[61] R. H. West, M. S. Celnik, O. R. Inderwildi, M. Kraft, G. J. O. Beran, W. H. Green, Toward a comprehensive model of the synthesis of TiO_2 particles from $TiCl_4$, Ind. Eng. Chem. Res. 46 (2007) 6147–6156, doi:10.1021/ie0706414.

[62] R. H. West, R. Shirley, M. Kraft, C. F. Goldsmith, W. H. Green, A detailed kinetic model for combustion synthesis of titania from $TiCl_4$, Combust. Flame 156 (2009) 1764–1770, doi:10.1016/j.combustflame.2009.04.011.

[63] J. Akroyd, A. J. Smith, R. Shirley, L. R. McGlashan, M. Kraft, A coupled CFD-population balance approach for nanoparticle synthesis in turbulent reacting flows, Chem. Eng. Sci. 66 (2011) 3792–3805, doi:10.1016/j.ces.2011.05.006.

[64] S. J. Harris, I. M. Kennedy, The coagulation of soot particles with van der Waals forces, Combust. Sci. Technol. 59 (1988) 443–454, doi: 10.1080/00102208808947110.

[65] R. I. A. Patterson, J. Singh, M. Balthasar, M. Kraft, W. Wagner, Extending stochastic soot simulation to higher pressures, Combust. Flame 145 (2006) 638–642, doi:10.1016/j.combustflame.2006.02.005.

[66] J. Arvo, Fast random rotation matrices, in: D. Kirk (Ed.), Graphics Gems III, Academic Press, 117–120, 1992.

[67] J. Ritter, An efficient bounding sphere, in: A. S. Glassner (Ed.), Graphics Gems, Academic Press, 301–303, 1990.

[68] T. Matsoukas, S. K. Friedlander, Dynamics of aerosol agglomerate formation, J. Colloid Interface Sci. 146 (1991) 495–506, doi:10.1016/0021-9797(91)90213-R.

[69] S. Tsantilis, S. E. Pratsinis, Soft- and hard-agglomerate aerosols made at high temperatures, Langmuir 20 (2004) 5933–5939, doi: 10.1021/la036389w.

[70] M. Lapuerta, R. Ballesteros, F. J. Martos, A method to determine the fractal dimension of diesel soot agglomerates, J. Colloid Interface Sci. 303 (2006) 149–158, doi:10.1016/j.jcis.2006.07.066.

[71] M. Astier, P. Vergnon, Determination of the diffusion coefficients from sintering data of ultrafine oxide particles., J. Solid State Chem. 19 (1976) 67–73, doi:10.1016/0022-4596(76)90151-1.

[72] H. U. Anderson, Initial sintering of rutile, J. Am. Ceram. Soc. 50 (1967) 235–238, doi:10.1111/j.1151-2916.1967.tb15094.x.

[73] S. Tsantilis, H. Briesen, S. E. Pratsinis, Sintering Time for Silica Particle Growth, Aerosol Sci. Technol. 34 (2001) 237–246, doi: 10.1080/02786820150217812.

[74] B. Buesser, A. J. Gröhn, S. E. Pratsinis, Sintering rate and mechanism of TiO_2 nanoparticles by molecular dynamics, J. Phys. Chem. C 115 (2011) 11030–11035, doi:10.1021/jp2032302.

[75] T. Seto, M. Shimada, K. Okuyama, Evaluation of sintering of nanometer-sized titania using aerosol method, Aerosol Sci. Technol. 23 (1995) 183–200, doi:10.1080/02786829508965303.

[76] A. Kobata, K. Kusakabe, S. Morooka, Growth and transformation of TiO$_2$ crystallites in aerosol reactor, AIChE J. 37 (1991) 347–359, doi: 10.1002/aic.690370305.

[77] M. Celnik, R. Patterson, M. Kraft, W. Wagner, Coupling a stochastic soot population balance to gas-phase chemistry using operator splitting, Combust. Flame 148 (2007) 158–176, doi: 10.1016/j.combustflame.2006.10.007.

[78] G. Strang, On the construction and comparison of difference schemes, SIAM J. Numer. Anal. 5 (1968) 506–517, doi:10.1137/0705041.

[79] S. N. Rogak, R. C. Flagan, H. V. Ngyyen, The mobility and structure of aerosol agglomerates, Aerosol Sci. Technol. 18 (1993) 25–47, doi: 10.1080/02786829308959582.

[80] M. Y. Manuputty, C. S. Lindberg, M. L. Botero, J. Akroyd, M. Kraft, Detailed characterisation of TiO$_2$ nano-aggregate morphology using TEM image analysis, Technical Report 213, c4e-Preprint Series, Cambridge .

[81] G. Sharma, S. Dhawan, N. Reed, R. Chakrabarty, P. Biswas, Collisional growth rate and correction factor for TiO$_2$ nanoparticles at high temperatures in free molecular regime, J. Aerosol Sci. 127 (2018) 27–37, doi:10.1016/j.jaerosci.2018.10.002.